ELSEVIER

Mechanics of Materials 29 (1998) 275–305

MECHANICS OF MATERIALS

Adaptive FEM computation of geometric and material nonlinearities with application to brittle failure

Horacio D. Espinosa *, Pablo D. Zavattieri, Gordon L. Emore

School of Aeronautics and Astronautics, Purdue University, West Lafayette, IN 47907-1282, USA

Received 10 August 1997; revised version received 15 August 1997

Abstract

A model is presented for the dynamic finite element analysis of large-strain, high strain rate deformation behavior of materials. A total Lagrangian formulation is used in the derivation of discrete equations of motion. Both an isochoric finite deformation plasticity model, including rate and temperature effects, for metals, and a multiple-plane microcracking model for ceramics are introduced. In addition, algorithms are presented for correcting finite element mesh distortion through mesh rezoning, optimization, and refinement. A surface-defined multibody contact algorithm designed to handle large relative displacements between bodies, with addition for friction, is included. Extensions of the mechanical contact to account for heat fluxes between sliding bodies and the treatment of body interfaces with cohesive strength are presented within a unified framework. Two test examples are examined, simulating a modified Taylor rod impact experiment, in which an aluminum anvil strikes a confined or unconfined ceramic rod. Axial and radial velocities are computed at the free end of the ceramic and at 30 mm from the impact surface, respectively. Comparisons with experimental traces reveal that the simulations produce the same overall features observed in the experimental data.

Keywords: Adaptive remeshing; Mesh optimization; Damage; Ceramics; Impact

1. Introduction

There is a class of applications in which material and geometric nonlinearities play a major role in understanding the physics of the problems. This group includes problems in high speed machining, metal forming, and impact-induced damage in ductile and brittle materials. What makes these problems special is the fact that the deformations involved are severe and also take place very quickly, resulting in large strains and strain rates, high temperatures and stresses, and unusual friction conditions. In machining, for example, the surfaces of workpieces have been estimated to have plastic strains as high as 500%, as seen in Komanduri (1993). Experimental observations of metal cutting operations show that deformations occur in concentrated regions, in which material is subjected to shear deformation at very high strain rates (10^3–10^5), Oxley (1989). A similar scenario is observed in impact and ballistic penetration (Zukas, 1990).

Experimental investigations show that material properties, such as stress-strain properties, are strongly affected by strain rate and temperature during plastic deformation (Duffy, 1979; Clifton and Klopp, 1985; Nicholas and Rajendran,

* Corresponding author. E-mail: espinosa@ecn.purdue.edu.

0167-6636/98/$ – see front matter
PII: S0167-6636(98)00018-0

1990). For the same strain, the corresponding stress increases with strain rate due to viscous effects. In addition, heat generated by plastic processes and friction increases the temperature of the material, leading to thermal softening which can result in material instabilities. Temperatures in excess to 600°C have been observed in machining experiments performed on 1020 steel (Shih and Yang, 1993). High temperatures resulting from plastic deformation were also measured within shear bands in maraging steel and Ti alloys, (Zhou et al., 1996).

In the case of brittle materials, ceramics, glasses, and ceramic composites, several failure modes have been proposed. The most widely accepted failure mechanisms are: microcracking, void collapse under compression, grain boundary shearing (in ceramics containing a glassy phase), twining and microplasticity. Many experimental configurations have been used to identify and quantify inelasticity in brittle materials. Shock wave experiments were performed by Rosenberg et al. (1985) and Longy and Cagnoux (1989), and Grady (1995). Normal impact *recovery* and pressure-shear experiments were performed by Espinosa et al. (1992), Espinosa and Clifton (1991) and Sundaram and Clifton (1996). Rod on Rod impact experiments (Simha et al., 1995; Wise and Grady, 1994; Espinosa and Brar, 1995) were also performed to identify damage initiation and evolution under two-dimensional loading conditions.

In general, physical experiments do not always provide direct information on material behavior and failure. Therefore, numerical simulations are useful in helping researchers to obtain insight into the physics of deformation and fracture of advanced materials. However, from a computational standpoint, the class of problems previously mentioned present several difficulties. Large relative deformations occur very quickly in well defined moving domains. Strain and temperature gradients can be extremely sharp requiring a high degree of spatial and temporal resolution of the field variables. Moreover, in the case of brittle materials, a transition from continuous damage to discrete fragmentation occurs. All these features constitute important challenges in the development of new computational capabilities.

Most FEM calculations for solid mechanics use a Lagrangian formulation (Belytschko, 1983; Benson, 1992). This means that as the mesh becomes deformed, errors may accumulate from highly distorted elements. A greatly deformed element may become unsuitable for further updates in the calculation, e.g., Yang et al. (1989), Batra and Kuo (1992) and Ortiz and Quigley (1991). In addition, as elements are distorted, the time step required for explicit integration algorithms (which are only conditionally stable) tends to dwindle such that completing a dynamic calculation may become extremely expensive from a computational view point (Espinosa et al., 1995). The initial mesh may also become inappropriate as time progresses, because high strain gradients may develop in areas of the mesh with insufficient resolution to accurately model geometric and material nonlinearities.

There are several methods for dealing with these problems. Highly distorted meshes may be fixed by moving and *optimizing* node locations, as in Zienkiewicz and Taylor (1991b). Nodes may also be moved closer to regions of interest using *adaptive meshing* algorithms. Several contributions have been made in this direction, e.g., Zhu et al. (1991) and Batra and Hwang (1993). Alternatively, a mesh may be replaced completely with a brand new mesh in an operation called *remeshing* or *rezoning*. Additional nodes may be added in regions of interest to produce more elements in an *h-refinement*, thereby creating more resolution where large temperature and displacement gradients are occurring (Marusich and Ortiz, 1995). Another way of dealing with mesh distortion is by using arbitrary Lagrangian–Eulerian (ALE) methods, (Donea, 1983; Liu et al., 1988; Benson, 1992; Dvorkin and Petocz, 1992). As featured in Stillman et al. (1993), the ALE method is able to continuously rebuild the boundaries in an Eulerian fashion, as part of the regular smoothing operation, resulting in good accuracy and reducing CPU time with respect to pure Lagrangian formulations.

The development of new and faster computers with parallel capabilities, as well as the manufacturing of ultra fast speed cameras, detectors, and oscilloscopes, open new frontiers for the investigation of the mechanics and material issues discussed

above. As an example of how experiments and numerical simulations are combined to examine material inelasticity and failure, we here present a finite element model to simulate dynamic contact, and geometric and material nonlinearities resulting from high speed impact. The model includes a temperature and strain-rate dependent material model for large deformation plasticity, microcracking for the case of brittle materials, and a multi-body contact law with a variable-coefficient friction law and heat conduction. In addition, the capability to rezone, refine, optimize, and update the finite element mesh is included to allow the calculation to continue in a timely fashion through extremely severe deformations. This is accomplished without resorting to numerical erosion schemes, as in other Lagrangian formulations, e.g., EPIC (1996), that can lead to results difficult to interpret or that fail to reproduce the physics of the problem. A good example of this type of problems, it is the so-called *interface defeat phenomenon*, which was experimentally discovered by Hauver et al. (1994) in their studies of ballistic penetration of ceramic targets. In this problem, tungsten heavy alloys (WHA) penetrators are defeated at a ceramic/metal interface through a mechanism of lateral plastic flow. Certainly, an erosion scheme would fail to simulate the large inelastic deformation of the WHA penetrator and its defeat.

In this paper, the features of the developed computational algorithms are illustrated by examining the high velocity impact of a T-shaped aluminum rod against unconfined and confined ceramic rods, Wise and Grady (1994). Interferometrically measured velocities are used to assess the quality of the proposed models.

2. The stress and deformation model

2.1. Field equations

In our formulation, the field equations describing the material response of a body use a total Lagrangian approach. Consider a solid with volume B_0 in the reference configuration, and a deformation process characterized by the mapping $\mathbf{x}(\mathbf{X}, t)$. Then a material point initially at $\mathbf{X}$ will be located at $\mathbf{x} = \mathbf{X} + \mathbf{u}$ after deformation, in which $\mathbf{u}$ is the displacement vector, as shown in Fig. 1. A displacement based finite element formulation is obtained from the weak form of the momentum balance or dynamic principle of virtual work. At time t, the weak form is given by

$$\int_{B_0} [\nabla_0 \mathbf{T}^0 + \rho_0(\mathbf{b}_0 - \mathbf{a})] \cdot \eta \, \mathrm{d}B_0 = 0, \tag{1}$$

$$\int_{B_0} \mathbf{T}^0 : \nabla_0 \eta \, \mathrm{d}B_0 - \int_{B_0} \rho_0(\mathbf{b}_0 - \mathbf{a}) \cdot \eta \, \mathrm{d}B_0 - \int_{S_{0\sigma}} \mathbf{t} \cdot \eta \, \mathrm{d}S_0 = 0, \tag{2}$$

where $\mathbf{T}^0$ is the first Piola–Kirchhoff stress tensor at time t; $\mathbf{b}_0$, $\mathbf{a}$, and $\mathbf{t}$ are the body force vector, acceleration vector, and boundary traction vector on volume B_0 and boundary $S_{0\sigma}$, respectively. Virtual displacement field η is assumed to be admissible, and ρ_0 represents the material density per unit volume in the reference configuration. The symbol ∇_0 denotes the material gradient with respect to the reference configuration, and ':' is used to denote the inner product between second order tensors, e.g., $\mathbf{A} : \mathbf{B} \equiv A_{ij}B_{ji}$, where the summation convention on repeated indices is implied. Another form of the weak form of the momentum balance, in terms of spatial quantities, is given by

$$\int_{B_0} \tau : \nabla^s \eta \, \mathrm{d}B_0 - \int_{B_0} \rho_0(\mathbf{b}_0 - \mathbf{a}) \cdot \eta \, \mathrm{d}B_0 - \int_{S_{0\sigma}} \mathbf{t} \cdot \eta \, \mathrm{d}S_0 = 0 \tag{3}$$

in which superscript s stands for the symmetric part of the tensor, $\tau = \mathbf{F}\mathbf{T}^0$ is the Kirchhoff stress,

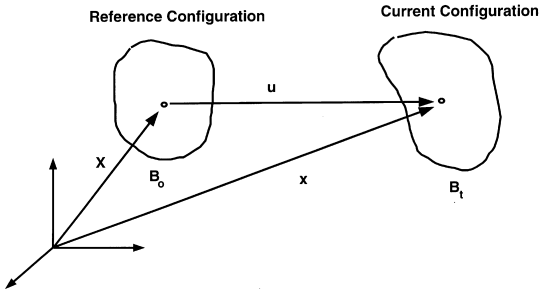

Fig. 1. Reference and current configurations.

$\mathbf{F}$ is the deformation gradient at time t, and ∇ is the spatial deformation tensor. As Eq. (3) shows, the equation of motion in its weak form states that the work done by the stresses τ over strains $\nabla^s\eta$ equals the work done by applied body forces, inertia forces, and surface tractions.

2.2. Large deformation plasticity model

The plasticity constitutive law used here is based on an atomic lattice model for metals to describe elastic and plastic material behavior. Consider a crystal lattice being deformed from its initial undeformed configuration B_0 to its current configuration B_t at time t. Locally, the deformation of the crystal is fully defined by the deformation gradient field $\mathbf{F}$. The total deformation $\mathbf{F}$ is the result of two main mechanisms of deformation: dislocation motion within the active slip systems of the crystal and lattice distortion. Following Lee (1969), this points to a multiplicative decomposition of the deformation gradient $\mathbf{F}$ into a plastic part $\mathbf{F}^p$, defined as the cumulative effect of dislocation motion, and an elastic part $\mathbf{F}^e$, which describes the distortion of the lattice. Namely,

$$\mathbf{F} = \mathbf{F}^e\mathbf{F}^p. \tag{4}$$

Following Teodosiu (1970), Rice (1971), Mandel (1972), Hill and Rice (1972), Havner (1973) and Asaro and Rice (1977), we shall assume that $\mathbf{F}^p$ leaves the crystal not only essentially undistorted, but also unrotated, as seen in Fig. 2. Thus, the rotation of the lattice is contained in $\mathbf{F}^e$. This choice of kinematics uniquely determines the decomposition (4). The plastic part $\mathbf{F}^p$ of the deformation gradient defines a collection of plastically deformed local configurations referred to as the intermediate configuration $\overline{B}_t$. Although this configuration is fictitious, it can be interpreted as the configuration obtained from macroscopic unloading, from the current configuration, in the absence of further motion of crystal defects, i.e., constant lattice structure.

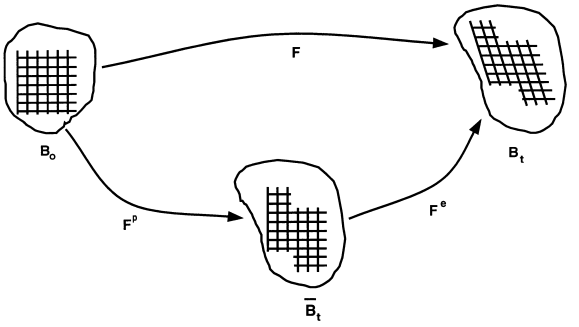

Fig. 2. Deformation gradient decomposition.

Insight into the structure of the constitutive relations can be obtained from work conjugacy considerations (Lubliner, 1990). By virtue of the decomposition (4), the deformation power per unit of undeformed volume takes the form

$$\mathbf{T}^0 : \dot{\mathbf{F}} = \overline{\mathbf{T}}^0 : \dot{\mathbf{F}}^e + \overline{\mathbf{\Sigma}} : \overline{\mathbf{L}}^p \tag{5}$$

or

$$\mathbf{S} : \dot{\mathbf{E}} = \overline{\mathbf{S}} : \dot{\mathbf{E}}^e + \overline{\mathbf{\Sigma}} : \overline{\mathbf{L}}^p, \tag{6}$$

where $\mathbf{T}^0$ is the first Piola–Kirchhoff stress tensor, $\mathbf{S}$ is the second Piola–Kirchhoff stress, $\mathbf{E}$ is the Lagrangian strain, and

$$\overline{\mathbf{T}}^0 = \mathbf{T}^0\mathbf{F}^{p\mathrm{T}}, \tag{7}$$

$$\overline{\mathbf{S}} = \mathbf{F}^p\mathbf{S}\mathbf{F}^{p\mathrm{T}}, \tag{8}$$

$$\overline{\mathbf{\Sigma}} = \mathbf{F}^{e\mathrm{T}}\mathbf{T}^0\mathbf{F}^{p\mathrm{T}} = \overline{\mathbf{C}}^e\overline{\mathbf{S}} = \mathbf{F}^{e^{\mathrm{T}}}\tau\mathbf{F}^{e-\mathrm{T}}, \tag{9}$$

$$\overline{\mathbf{L}}^p = \dot{\mathbf{F}}^p\mathbf{F}^{p-1}. \tag{10}$$

Here, $\overline{\mathbf{T}}^0$ defines a first Piola–Kirchhoff stress tensor relative to the intermediate configuration $\overline{B}_t$, $\overline{\mathbf{S}}$ defines a second Piola–Kirchhoff stress tensor relative to the intermediate configuration $\overline{B}_t$, $\overline{\mathbf{C}}^e = \mathbf{F}^e\mathbf{F}^{e\mathrm{T}}$ is the elastic right Cauchy–Green deformation tensor in the intermediate configuration $\overline{B}_t$, and $\overline{\mathbf{\Sigma}}$ is a stress measure conjugate to the plastic velocity gradients $\overline{\mathbf{L}}^p$ on $\overline{B}_t$ (Mandel, 1972).

The work conjugacy relations expressed in Eqs. (5) and (6) suggest plastic flow rules and elastic stress-strain relations of the general form,

$$\overline{\mathbf{L}}^p = \overline{\mathbf{L}}^p(\overline{\mathbf{\Sigma}}, \overline{\mathbf{Q}}), \tag{11}$$

$$\overline{\mathbf{T}}^0 = \overline{\mathbf{T}}^0(\mathbf{F}^e). \tag{12}$$

Here, $\overline{\mathbf{Q}}$ denotes some suitable set of internal variables defined on the intermediate configuration, for which suitable equations of evolution, or hard-

ening laws, are to be supplied. It should be noted that Eq. (11) determines uniquely both the plastic deformation and the rate of plastic rotation. Because, by the choice of kinematics, $\mathbf{F}^p$ is invariant with respect to rigid body motions superimposed on the current configuration, Eq. (11) is automatically material frame indifferent. By contrast, objectivity imposes non-trivial restrictions on the form of Eq. (12). The most general form of Eq. (12) consistent with the principle of material frame indifference is

$$\overline{\mathbf{T}}^0 = \mathbf{F}^e \overline{\mathbf{S}}(\overline{\mathbf{C}}^e). \tag{13}$$

Several choices are available in the formulation of the above elasticity constitutive law. One law suitable for metals and polymers, up to moderately large elastic strains, was proposed by Weber and Anand (1990),

$$\overline{\mathbf{S}} = L(0.5 \ \ln \ \overline{C}^e) = L\overline{\mathbf{H}}^e, \tag{14}$$

where $\overline{\mathbf{H}}^e$ is a logarithmic strain measure or Henky strain and L the material stiffness fourth order tensor. For an elastic isotropic solid L is given by

$$\mathbf{L} = 2\mu\mathbf{I} + (k - \tfrac{2}{3}\mu)\mathbf{1} \otimes \mathbf{1}, \tag{15}$$

in which μ is the shear modulus, k the bulk modulus, $\mathbf{I}$ the identity fourth order tensor, and $\mathbf{1}$ the unity vector.

It should be pointed out that, in general, the choice of stress and strain measures in the formulation of constitutive laws is not unique and, in a sense, arbitrary. The only requirement is that in the computation of work, conjugate variables are used, as discussed previously. Moreover, for the logarithmic (Henky) strain, the work conjugate stress is the back rotated Cauchy stress tensor, $\overline{\tau} = J\mathbf{R}^{e\mathrm{T}}\sigma\mathbf{R}^e$, see Atluri (1984) and Bathe (1996). In the last equation, $\mathbf{R}^{\mathrm{e}}$ is the rotation tensor obtained from a polar decomposition of $\mathbf{F}^e$ and $J = \det \mathbf{F}$ is the jacobian.

In summary, the elastic and plastic portions of the deformation are separated by the multiplicative decomposition $\mathbf{F} = \mathbf{F}^{\mathrm{e}}\mathbf{F}^{\mathrm{p}}$ as outlined above, subjected to the restrictions $\det \mathbf{F}^e > 0$ and $\det \mathbf{F}^p = 1$. Moreover, from Eq. (10) it can be seen that the evolution equation for $\mathbf{F}^{\mathrm{p}}$ follows the flow rule

$$\dot{\mathbf{F}}^p = \overline{\mathbf{L}}^p \mathbf{F}^p, \tag{16}$$

$$\overline{\mathbf{L}}^p = \mathbf{W}^p + \mathbf{D}^p, \tag{17}$$

wherein $\overline{\mathbf{L}}^p$ is the plastic part of the velocity gradient $\overline{\mathbf{L}}$. Assuming that $\mathbf{W}^p \equiv \mathrm{skw}\ \overline{\mathbf{L}}^p = 0$ and that $\mathbf{D}^p \equiv \mathrm{sym}\ \overline{\mathbf{L}}^p = \mathbf{D}^p(\overline{\mathbf{S}}, \overline{\mathbf{Q}}) = \dot{\boldsymbol{\epsilon}}^p \overline{\mathbf{N}}$, the evolution law becomes, $\dot{\mathbf{F}}^p \mathbf{F}^{p^{-1}} = \dot{\boldsymbol{\epsilon}}^p \overline{\mathbf{N}}$. A nonzero plastic spin tensor has been proposed by several investigators. Numerical simulations show that nonzero plastic spins can lead to a more accurate representation of large plastic deformation in shear bands and other material instabilities. However, mesh adaptivity was not used in these studies. In the above expression of $\mathbf{D}^{\mathrm{p}}$, $\overline{\mathbf{N}}$ is the plastic flow direction and $\dot{\boldsymbol{\epsilon}}^{\mathrm{p}}$ is the effective plastic strain rate. Within a J2-flow formulation, the plastic flow direction is given as a function of the deviatoric part of the second Piola–Kirchhoff stress tensor, $\overline{\mathbf{S}}_{\mathrm{dev}}$, and the effective stress defined by

$$\overline{\mathbf{N}} = \frac{3}{2}\frac{\overline{\mathbf{S}}_{\mathrm{dev}}}{\overline{\sigma}}, \tag{18}$$

$$\overline{\sigma} = \sqrt{\tfrac{3}{2}\overline{\mathbf{S}}_{\mathrm{dev}} : \overline{\mathbf{S}}_{\mathrm{dev}}}. \tag{19}$$

The effective plastic strain rate, $\dot{\boldsymbol{\epsilon}}^p$, is a function of the effective stress $\overline{\sigma}$, temperature T, and the internal variables $\overline{\mathbf{Q}}$, viz.,

$$\dot{\boldsymbol{\epsilon}}^p = f(\overline{\sigma}, \overline{\mathbf{Q}}, T). \tag{20}$$

For a viscoplastic model, a common representation of this function is,

$$\dot{\boldsymbol{\epsilon}}^p = \dot{\boldsymbol{\epsilon}}_0^p \left[\left(\frac{\overline{\sigma}}{s(\boldsymbol{\epsilon}^p, T)} \right)^{\alpha} - 1 \right], \quad \overline{\sigma} > \mathbf{s}, \tag{21}$$

$$\dot{\boldsymbol{\epsilon}}^p = 0, \quad \overline{\sigma} \leqslant \mathbf{s}, \tag{22}$$

$$s(\boldsymbol{\epsilon}^p, T) = \sigma_0 \left(1 + \frac{\boldsymbol{\epsilon}^p}{\boldsymbol{\epsilon}_0^p} \right)^{1/\beta} \left[1 - \left(\frac{T - T_0}{T_{\mathrm{m}} - T_0} \right)^{\gamma} \right], \tag{23}$$

such that $\boldsymbol{\epsilon}^p$ is the accumulated plastic strain, σ_0 the initial material strength, T_{m} the melting temperature of the material, T_0 the reference temperature, and α, β, and γ are the rate sensitivity, hardening, and thermal softening exponents. The material strength $\mathbf{s}$ and ϵ^p are internal variables contained in $\overline{\mathbf{Q}}$. In this model the equations of evolution of the internal variables are defined by a

Table 1
Numerical integration algorithm

Constitutive	$\Longleftrightarrow$	Incremental
$\mathbf{F}=\mathbf{F}^e\mathbf{F}^p$	$\Longleftrightarrow$	$\mathbf{F}_{n+1}=\mathbf{F}^e_{n+1}\mathbf{F}^p_{n+1}$
$\dot{\mathbf{F}}^p\mathbf{F}^{p-1}=\dot{\boldsymbol{\epsilon}}^p\overline{\mathbf{N}}(\overline{\mathbf{S}},\overline{\mathbf{Q}})$	$\Longleftrightarrow$	$\mathbf{F}^p_{n+1}=\exp(\Delta\boldsymbol{\epsilon}^p\overline{\mathbf{N}}_{n+1})\mathbf{F}^p_n$
$\overline{\mathbf{S}}=L(\frac{1}{2}\ \ln\ \mathbf{C}^e)$	$\Longleftrightarrow$	$\overline{\mathbf{S}}_{n+1}=L(\frac{1}{2}\ \ln\ \mathbf{C}^e_{n+1})$
$\dot{\overline{\mathbf{Q}}}=\dot{\boldsymbol{\epsilon}}^p\mathbf{H}(\overline{\mathbf{S}},\overline{\mathbf{Q}})$	$\Longleftrightarrow$	$\overline{\mathbf{Q}}_{n+1}=\overline{\mathbf{Q}}_n+\Delta\boldsymbol{\epsilon}^p\overline{\mathbf{H}}_{n+1}$

tensor value function $\overline{\mathbf{H}}(\overline{\mathbf{S}},\overline{\mathbf{Q}})$, describing hardening/softening laws. A summary of the constitutive model and its discrete counterpart is given in Table 1. It should be noted that the exponential law discussed in the work by Weber and Anand (1990), is used to update the plastic part of the deformation gradient, $\mathbf{F}^p_{n+1}$.

2.3. Multiple-plane microcracking model

In this section, the inelastic response of ceramics is modeled through a microcracking multiple-plane model based on a dilute approximation (Taylor model). The formulation overlaps with some theories in which multiple-plane representations of inelasticity are derived, e.g., Seaman and Dein (1983), Bazant and Gambarova (1984) and Ju and Lee (1991).

The basic assumption in the microcracking multiple-plane model is that microcracking and/or slip can occur on a discrete number of orientations (see Fig. 3). Slip plane properties (friction, initial size, density, etc.) and their evolution are *independently* computed on each plane. The macroscopic response of the material is based on an additive decomposition of the strain tensor into an elastic part and an inelastic contribution arising from the presence of microcracks within the solid. In contrast to scalar representations of damage, e.g., Rajendran (1992), the formulation by Espinosa (1995) is broad enough to allow the examination of *damage induced anisotropy* and damage localization in the interpretation of impact experiments.

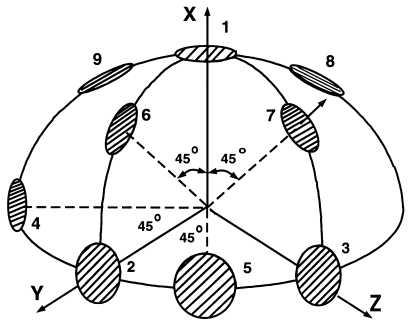

Fig. 3. Schematic of microcracking multiple-plane model.

For a representative volume B of an elastic solid containing penny-shaped microcracks with a density $N^{(k)}$, the average inelastic strains are given by

$$\epsilon^c_{ij}=\sum_{k=1}^{9}N^{(k)}A^{(k)}\frac{1}{2}(\overline{b}^{(k)}_i n^{(k)}_j+n^{(k)}_i\overline{b}^{(k)}_j), \tag{24}$$

where the subindex k is used to label the orientations, $A^{(k)}$ denotes the surface of a microcrack on orientation k, $n^{(k)}$ the corresponding unit normal, and $\overline{b}^{(k)}$ the average displacement jump vector across $A^{(k)}$.

If the resolved normal traction acting on the microcracks on orientation k is tensile, the average displacement jump vector resulting from an applied Cauchy stress field σ is given by

$$\overline{b}^{(k)}_i=\frac{1}{A^{(k)}}\int_{A^{(k)}}b^{(k)}_i\ \mathrm{d}A=\frac{16(1-v^2)}{3E(2-v)}a^{(k)}(2\sigma_{ij}n^{(k)}_j-v\sigma_{jl}n^{(k)}_j n^{(k)}_l n^{(k)}_i), \tag{25}$$

in which E and v are the Young's modulus and Poisson's ratio of the uncracked solid, and a^k is the radius of the penny-shaped microcracks on orientation k. By contrast, if the normal traction is compressive, the microcracks are closed and the average displacement jump is given by

$$\overline{b}^k_i=\frac{32(1-v^2)}{3\pi E(2-v)}a^k f^k_i, \tag{26}$$

where $\mathbf{f}^k$ is the effective shear traction vector on orientation k given by

$$f^k_i=(\tau^k+\mu\sigma^k_n)(n_\tau)^k_i. \tag{27}$$

In Eq. (27), μ is the friction coefficient of the microcrack faces, τ^k and σ^k_n are the resolved shear stress and the normal stress acting on microcracks with orientation k, respectively, and n^k_τ is the unit vector in the direction of the resolved shear traction. Embodied in 26 is the notion that f^k provides the effective driving force for the sliding of the microcracks.

In order to compute the inelastic strain tensor at all times, it becomes necessary to follow the evolution of the microcrack radius a^k in the selected orientations. Following Freund (1990), an equation of evolution for a in the case of mixed mode loading can be derived (Espinosa, 1995), viz.,

$$\dot{a}^k = m^{\pm} c_R [1 - (K_{IC}/K^k_{eff})^{n^{\pm}}] \geqslant 0, \tag{28}$$

in which $n^{\pm}$ and $m^{\pm}$ are phenomenological material constants which may have different values in tension and compression, c_R is the Rayleigh wave speed, K_{IC} is the material toughness, and K^k_{eff} is an effective stress intensity factor. For mixed mode conditions, K^k_{eff} is derived by considering an average energy release rate associated with an increase in radius of the microcracks, namely,

$$\mathscr{G}^k = \frac{1}{2\pi}\int_0^{2\pi} \frac{1-\nu^2}{E}\left[K_I^2 + K_{II}^2 + K_{III}^2/(1-\nu)\right] d\theta \tag{29}$$

from which the following expression for K^k_{eff} is obtained,

$$K^k_{eff} = \sqrt{\frac{\mathscr{G}^k E}{1-\nu^2}}. \tag{30}$$

The general structure of these constitutive equations corresponds to that of a solid with a damage-induced anisotropic stress-strain relation with elastic degradation. In particular, the effective behavior of the solid is predicted to be rate dependent due to crack kinetics effects. From a computational standpoint, this insures numerical reliability and mesh independence, according to Needleman (1988), and Espinosa (1989). This is in contrast to quasi-static formulations of damage for which the governing equations become ill-posed in the softening regime, as in Sandler and Wright (1984). Details about the stress update algorithm, assuming an additive decomposition of strain rates into an elastic and cracking part, can be found in Espinosa (1995).

It should be pointed that this inelastic model is a *continuum* model in which material damage results from microcracking. If the material is subjected to a predominantly tensile stress state, microcracks along orientations perpendicular to the direction of maximum tensile stresses will grow according to Eq. (5). In this case, significant dilation is expected due to mode I crack opening. If a predominantly compressive state of stress with shear is imposed, then crack opening is inhibited but inelasticity is manifested by the growth of penny-shaped cracks in modes II and III (shear modes).

2.4. Finite element discretization

Discretization of Eq. (3) defines a system of nonlinear ordinary differential equations which can be solved for the updated deformation $\mathbf{x}_{n+1}$. A displacement-based finite element formulation is obtained by expressing field variables at any point in an element as a function of nodal quantities and the element shape functions in the reference configuration:

$$u_{ia} = \sum_{a=1}^{NEN} N_a(\xi) u_i^a, \tag{31}$$

$$v_{ia} = \sum_{a=1}^{NEN} N_a(\xi) v_i^a, \tag{32}$$

$$a_{ia} = \sum_{a=1}^{NEN} N_a(\xi) a_i^a, \tag{33}$$

wherein u_{ia}, v_{ia}, and a_{ia} are the displacement, velocity, and acceleration at the point of interest. The sum is taken over the number of nodes in the element, NEN, while $N_a(\xi)$ are the shape functions relating nodal quantities u_i^a, v_i^a, and a_i^a to the point of interest. The vector ξ contains the natural coordinates of the point of interest in the isoparametric master element. Substitution of the discretized variables into Eq. (3) leads to the following system of ordinary differential equations,

$$M_{iajb} a_{jb} = f^{ext}_{ia} - f^{int}_{ia} \tag{34}$$

$$f^{int}_{ia} = \sum_e \int_{B_0^e} n_{a,j} \tau_{ij} \, dB_0 = \sum_e \int_{B_0^e} \mathbf{B}^T \tau \, dB_0 \tag{35}$$

$$f^{ext}_{ia} = \sum_e \int_{B_0^e} \rho_0 b_{0i} N_a^e \, dB_0 + \int_{\partial S_0^e} \bar{t}_i N_a \, dS_0 \tag{36}$$

$$M_{iajb} = \sum_e \int_{B_0^e} \delta_{ij}\rho_0 N_b^e N_a^e \, \mathrm{d}B_0, \tag{37}$$

in which f_{ia}^{int}, f_{ia}^{ext}, and M_{iajb} are the internal nodal forces, the external nodal forces, and the lumped mass matrix, respectively. In order to obtain a uniform mass distribution in the mesh, the element mass was lumped proportional to the angles defined in Fig. 4. For a typical node a we have

$$M_{iaia} = \sum_{i=1}^{\mathrm{NEL}} \sum_k \rho_0 a_k^l \theta_k^l / \pi. \tag{38}$$

Areas a_k and angles θ_k are defined in Fig. 4. Subscript k runs from 1 to 3 for midside nodes and is 1 for corner nodes. In the above equation, NEL is the number of elements sharing node a.

The integrations of the body forces, inertia forces, and stress contributions take place over an element volume B_0^e, while the applied tractions are integrated over the element surface ∂S_0^e. Dynamic equilibrium requires that internal and external forces are balanced by the inertia forces. The shape function derivatives $n_{a,j}$ are defined in the current configurations. The body forces and surface tractions are applied upon the volume B_0, and surface ∂S_0^e. In the expression for f_{ia}^{int}, the Kirchoff stress can be expressed in terms of the second Piola–Kirchhoff stress tensor $\overline{\mathbf{S}}$ in the intermediate configuration, and the elastic part of the deformation gradient, $\mathbf{F}^{\mathrm{e}}$, namely,

$$\boldsymbol{\tau} = \mathbf{F}^{\mathrm{e}}\overline{\mathbf{S}}\mathbf{F}^{\mathrm{eT}}. \tag{39}$$

2.5. Direct time integration algorithm

An explicit central-difference integration algorithm is being used to integrate the system of ordinary differential equations in time. The algorithm, accounting for acceleration corrections due to contact, is summarized in Table 2. As in any initial boundary value problem, initial displacements and velocities $\mathbf{u}^0$ and $\mathbf{v}^0$ are required. Initial accelerations $\mathbf{a}_0$ are calculated from initial applied forces $\mathbf{f}_0^{\mathrm{ext}}$, and initial internal forces $\mathbf{f}_0^{\mathrm{int}}$.

At each time step n, the nodal accelerations must first be corrected for any time-dependent changes in the traction boundary conditions. Then a displacement predictor at time $n+1$, is computed using the corrected acceleration and the displacements and velocities at time step n. Modified accelerations at time n are computed based on the corrected acceleration and changes in accelerations resulting from surface contact determined from the displacement predictor at $n+1$. Updated displacements at $n+1$ are used in the update of stresses and the computation of internal forces. Lastly, accelerations and velocities at time $n+1$ are obtained completing the time integration scheme.

This explicit integration method is very useful for studies in which high rates of loading are expected. The time steps used by these explicit calcu-

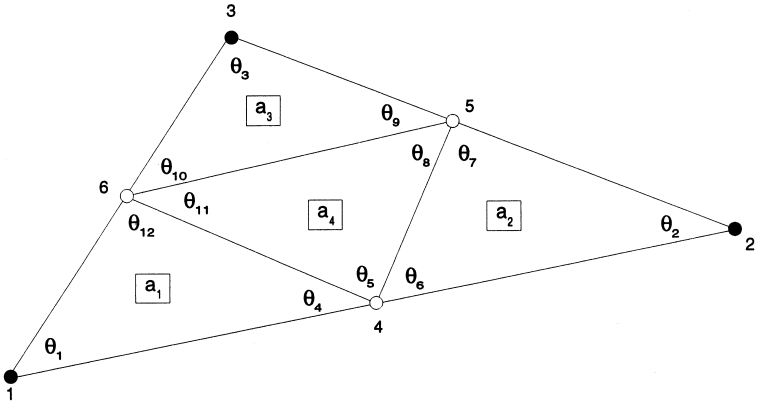

Fig. 4. Typical element partition for lumped mass calculation.

Table 2
Explicit integration algorithm

1. Initial conditions:

$n = 0$

$\mathbf{u}_0 = \bar{\mathbf{u}}_0$

$\mathbf{v}_0 = \bar{\mathbf{v}}_0$

$\mathbf{a}_0 = \mathbf{M}^{-1}(\mathbf{f}_0^{\text{ext}} - \mathbf{f}_0^{\text{int}})$.

2. Correct accelerations due to changes in boundary conditions:

$\hat{\mathbf{a}}_n = \mathbf{M}^{-1}(\mathbf{f}_{n+1}^{\text{ext}} - \mathbf{f}_n^{\text{ext}})$.

3. Compute displacement predictor:

$\hat{\mathbf{u}}_{n+1} = \mathbf{u}_n + \Delta t \mathbf{v}_n + \frac{1}{2}\Delta t^2 \hat{\mathbf{a}}_n$.

4. Modify accelerations due to surface contact based on $\hat{\mathbf{u}}_{n+1}$:

$\mathbf{a}_n = \hat{\mathbf{a}}_n + \Delta \mathbf{a}_n$

5. Update displacements:

$\mathbf{u}_{n+1} = \mathbf{u}_n + \Delta t \mathbf{v}_n + \frac{1}{2}\Delta t^2 \mathbf{a}_n$.

6. Update second Piola–Kirchhoff stress tensor $\bar{\mathbf{S}}$ at each element (see Table 1).

7. Compute internal force vector:

$\mathbf{f}_{n+1}^{\text{int}} = \int_{B_0} \mathbf{B}^{\mathrm{T}} \tau_{n+1} \, \mathrm{d}B_0; \qquad \tau_{n+1} = \mathbf{F}_{n+1}^{\mathrm{e}} \bar{\mathbf{S}}_{n+1} \mathbf{F}_{n+1}^{\mathrm{eT}}$.

8. Solve for accelerations:

$\mathbf{a}_{n+1} = \mathbf{M}^{-1}(\mathbf{f}_{n+1}^{\text{ext}} - \mathbf{f}_{n+1}^{\text{int}})$.

9. Update velocity vector:

$\mathbf{v}_{n+1} = \mathbf{v}_n + \frac{\Delta t}{2}(\mathbf{a}_n + \mathbf{a}_{n+1})$.

10. $n = n + 1$, if $n < n_{\max}$ go to step 2, else stop.

lations are limited by stability, so care must be taken in finite deformation dynamic calculations to ensure that waves do not propagate through the mesh faster than the material wave speeds. To this end, the time step is calculated dynamically from the maximum element frequency in the mesh $\omega_{\max}$, such that $\Delta t \leqslant 2/\omega_{\max}$. Flanagan and Belytschko (1984) derived the following estimate of $\omega_{\max}$ for an N-noded isoparametric element,

$$\omega_{\max}^2 \leqslant N \left(\frac{\hat{\lambda} + 2\hat{\mu}}{\rho} \right) \frac{B_{iI} B_{iI}}{A^2}, \tag{40}$$

in which $B_{iI}B_{iI}$ is the trace of $[B][B]^{\mathrm{T}}$, and the area A_0 is found as $C_{IJ}X_I Y_J$, where

$$C_{IJ} = \int\int_A \left(\frac{\partial N_I}{\partial \xi}\frac{\partial N_J}{\partial \eta} - \frac{\partial N_I}{\partial \eta}\frac{\partial N_J}{\partial \xi} \right) \mathrm{d}\eta \, \mathrm{d}\xi, \tag{41}$$

and N_I are the element shape functions. For the case of a 6-noded isoparametric triangular element, C_{IJ} is computed to be the 6×6 matrix

$$C_{IJ} = \frac{1}{6} \begin{pmatrix} 0 & 3 & 7 & 10 & -10 & -10 \\ -3 & 0 & -7 & -10 & 10 & 10 \\ -7 & 7 & 0 & 0 & -8 & 8 \\ -10 & 10 & 0 & 0 & -8 & 8 \\ 10 & -10 & 8 & 8 & 0 & -16 \\ 10 & -10 & -8 & -8 & 16 & 0 \end{pmatrix}. \tag{42}$$

3. Mechanical contact

Contact algorithms allow the study of complex interactions between bodies as occurs in many practical applications such as impact and surface machining. An algorithm, particularly suitable to explicit time integrators was developed by Taylor and Flanagan (1987). The 2-D version of the algorithm is here discussed. Extensions to account for heat flux between contact surfaces and the treatment of cohesive interfaces are presented in subsequent sections. The algorithm consists in predicting accelerations assuming no contact and later on correcting the accelerations of the surface nodes so that the surfaces do not interpenetrate. In addition, a velocity-dependent friction model is included. This surface-based contact algorithm allows contact between bodies that undergo large relative displacements as they move. It also allows the easy incorporation of a velocity-dependent friction model where the friction coefficient is made a function of pressure and temperature. In this section we start with a description of the contact algorithm as presented in Taylor and Flanagan (1987), followed by an extension to model cohesive interfaces.

3.1. Surface definition

The contact algorithm must keep track of the relative positions of the two surfaces. This requires

the storage of an array listing the surface nodes for each body. In our FEM code, which is a modified version of the Finite Element Analysis Program, FEAP, Zienkiewicz and Taylor (1991a), the mesh is generated in blocks, and a subroutine is called to generate the needed arrays of surface nodes. To begin with, a surface definition routine identifies all element corner nodes on the surface of the block. This is currently done in a loop over all of the elements, wherein each corner node accumulates the difference between the node numbers of the other two corner nodes. The end result of this is that all interior corner nodes accumulate a sum of zero, while the boundary corner nodes have a nonzero sum. Then, starting with the first boundary corner node, the algorithm examines the elements attached to the node to find the next corner node on the boundary, in a counter-clockwise direction. This is easily enough done as the element connectivities are also defined in a counter-clockwise direction. As each new boundary corner node is added to the surface array, the midnode between it and the previous node is also added. The algorithm repeats the process until it returns to the starting point.

3.2. Surface tracking

With every time step, the contact algorithm first must predict the accelerations, velocities, and displacements for the next time step. Our version of FEAP obtains these data ($\hat{\mathbf{a}}$, $\hat{\mathbf{v}}$, $\hat{\mathbf{u}}$,) from the explicit integration routine that precedes it. The resulting displacements are then used to determine whether or not contact has taken place.

During each time step, one of the surfaces is designated as *master* surface, and the other as *slave* surface. The algorithm assumes that slave nodes can be penetrating the faces between the master nodes. Therefore, an array is updated every time step by moving from a previous closest master node to a closer adjacent master node. Then the process is repeated until no adjacent node is closer. This method allows gradual relative motion between the two surfaces, while reducing the chances of sudden jumps across the material near sharp corners.

3.3. Determining contact

Once the appropriate master node is chosen, the position of the slave node is compared to the faces on either side of the master node. For a 2-D implementation, these two faces are the lines connecting the closest master point and the master nodes preceding and following it, respectively. The slave node is projected onto each of these lines to determine whether or not it falls within the influence of either or both of the two faces.

First of all, the angle between the master faces is bisected, and the location of the slave node with respect to the bisector is used to determine which master face is *near*, and which is *far*. The *near* face is the one which lies on the same side of the bisector as the slave node. Several tests are now made to determine if contact has occurred, as detailed in Figs. 5 and 6. They hinge upon several definitions. The slave node is considered to be *penetrating* a face if the dot product between the projection vector from the slave node to the surface and the master surface normal is positive. The slave node is considered to be *along* a face if the above projection vector intersects the line defined by the face on the same side of the angle bisector as the face itself. The *opposing slave segment* is the face on the slave surface (adjacent to the slave node) that has the most negative dot product of its normal with respect to the master face normals. Finally, the opposing slave segment is *more opposed* to the master face that supplies the most negative dot product of the normals.

3.4. Acceleration corrections

To ensure that the two surfaces do not interpenetrate, any penetrating slave node and its associated masters must have accelerations applied to them to negate the predicted penetration. First, the penetration force of the slave node is calculated by

$$\mathbf{f}_p = -\frac{\beta m_s \delta}{\Delta t^2}\mathbf{n} \tag{43}$$

in which m_s is the mass of the slave node, δ the penetration distance, Δt the time step, and $\mathbf{n}$ the master surface normal vector. Parameter $0 < \beta < 1$

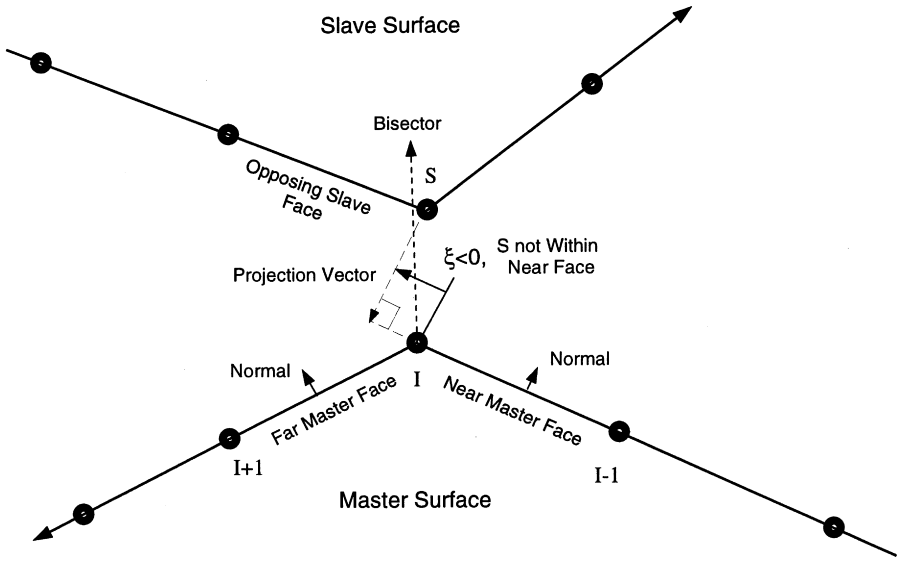

Fig. 5. Two surfaces are tested for contact.

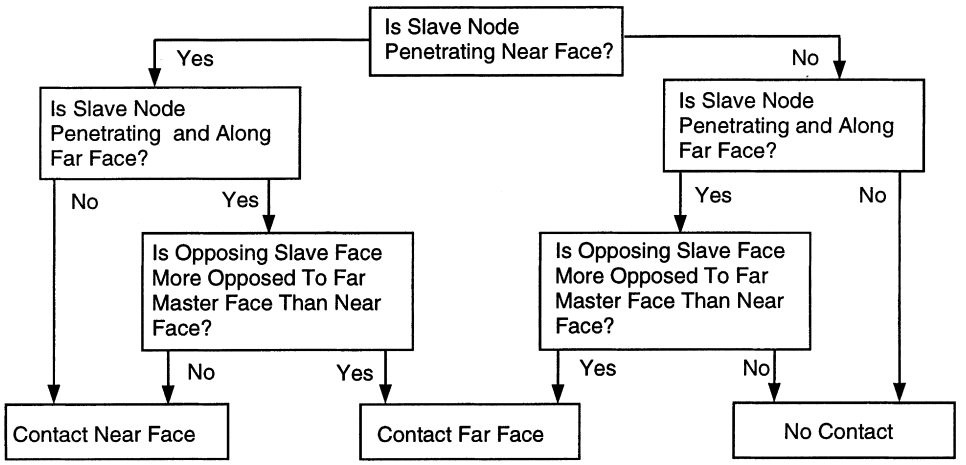

Fig. 6. Contact determination algorithm.

represents the fraction of a time step that a surface spends as a slave or master surface. For best results, similar materials should spend approximately equal amounts of time as slave and master surfaces, as master surfaces behave more stiffly than the slave surface.

Next, this force is balanced to the master nodes using the variable ξ, distance from the first node of the contact face to the projection point, non-dimensionalized by the length of the face. Once this is complete, the contributions are summed and virtual work is used to generate the acceleration correction for the master nodes:

$$m_{s1} = (1 - \xi)m_s, \tag{44}$$

$$m_{s2} = \xi m_s, \tag{45}$$

$$\mathbf{f}_{s1} = (1 - \xi)\mathbf{f}_p, \tag{46}$$

$$\mathbf{f}_{s2} = \xi \mathbf{f}_p, \tag{47}$$

$$\left(m+\sum_s m_{sI}\right)\mathbf{a}_{\mathbf{n}I}=\sum_s \mathbf{f}_{sI}. \tag{48}$$

In the above equation, the summation is over the contributions from the slave nodes contacting master node I. The correction for the slave node is then calculated using the master node responses, and is in turn used to get the final normal accelerations in the absence of friction for the slave and master nodes.

$$\mathbf{a}_{ns}=(1-\xi)\mathbf{a}_{n1}+\xi\mathbf{a}_{n2}, \tag{49}$$

$$\mathbf{a}_{\text{slv}}=\hat{\mathbf{a}}+\mathbf{a}_{ns}-\frac{\mathbf{f}_p}{m_s}, \tag{50}$$

$$\mathbf{a}_{\text{mstr}}=\hat{\mathbf{a}}+\mathbf{a}_{nI}. \tag{51}$$

3.5. Friction

Friction forces are handled by a velocity-dependent model, in which they resist the relative in-plane motion of the contacting surfaces. The relative velocity between the slave node and the corresponding master surface is calculated by

$$\hat{\mathbf{v}}_r=\hat{\mathbf{v}}_s-(1-\xi)\hat{\mathbf{v}}_1-\xi\hat{\mathbf{v}}_2 \tag{52}$$

wherein $\hat{\mathbf{v}}_s$, $\hat{\mathbf{v}}_1$, and $\hat{\mathbf{v}}_2$ are the predicted velocities for the slave node and the two master nodes, respectively. From this, the relative tangential velocity, $\mathbf{v}_s$, its magnitude v_s, and the tangential unit vector $\mathbf{s}$ can be found by

$$\hat{\mathbf{v}}_s=\hat{\mathbf{v}}_r-(\mathbf{n}\cdot\hat{\mathbf{v}}_r)\mathbf{n}, \tag{53}$$

$$v_s=\sqrt{\hat{\mathbf{v}}_s\cdot\hat{\mathbf{v}}_s}, \tag{54}$$

$$\mathbf{s}=\frac{\hat{\mathbf{v}}_s}{v_s}. \tag{55}$$

Similarly to the treatment of penetration, a tangential contact force defined as a fraction of the force that must be applied to the slave node to cancel its relative motion is given by

$$f_s=-\frac{\beta m_s v_s}{\Delta t}. \tag{56}$$

A key aspect in the treatment of contact is the definition of a friction coefficient. In general, the friction coefficient is a function of pressure, sliding velocity, and interface temperature. In what follows, we introduce a friction coefficient that is a function of the sliding velocity v_s, namely,

$$\mu=\mu_\infty+(\mu_0-\mu_\infty)\mathrm{e}^{-\gamma v_s} \tag{57}$$

in which μ_0 and μ_∞ are the low and high-velocity friction coefficients, and γ is a decay constant. Additional acceleration corrections are then calculated by

$$a_s=-\min\left(\mu(\mathbf{a}_{ns}-\frac{\mathbf{f}_p}{\mathbf{m}_s})\cdot\mathbf{n},\frac{\beta v_s}{\Delta t}\right), \tag{58}$$

$$\mathbf{a}_{\text{slv}}=\mathbf{a}_{\text{slv}}+a_s\mathbf{s}, \tag{59}$$

$$\mathbf{a}_{\text{mstr}_1}=\mathbf{a}_{\text{mstr}_1}-(1-\xi)\frac{a_s m_s}{m_1}\mathbf{s}, \tag{60}$$

$$\mathbf{a}_{\text{mstr}_2}=\mathbf{a}_{\text{mstr}_2}-\xi\frac{a_s m_s}{m_2}\mathbf{s}. \tag{61}$$

3.6. A dynamic interface/contact model

Recently, Espinosa and Lu (1995), proposed an extension of the above contact algorithm to model the dynamic behavior of interfaces. The motivation for this extension is to develop computational tools that can address problems such as dynamic delamination in composite materials, discrete fragmentation of brittle materials, and analysis of material microstructures where dynamic intergranular and intragranular fracture occurs.

The model is based on the interface model proposed by Tvergaard (1990), for quasi-static calculations and assumes that the interface carries forces that oppose separation and shear between two surfaces until debonding. The magnitude of these forces are a function of the relative separation and shear displacement between the two surfaces. The normal and tangential displacement jumps u_n and u_t, respectively, are used to determine a nondimensional parameter λ, defined as

$$\lambda=\sqrt{\left(\frac{u_n}{\delta_n}\right)^2+\left(\frac{u_t}{\delta_t}\right)^2}, \tag{62}$$

where δ_n and δ_t are the relative displacement components at which interface separation or debond-

ing takes place. Then, the interface traction vector may be calculated by

$$T_n = \frac{u_n}{\delta_n} F(\lambda), \qquad T_t = \alpha \frac{u_t}{\delta_t} F(\lambda), \tag{63}$$

$$F(\lambda) = \frac{27}{4}\sigma_{\max}(1 - 2\lambda + \lambda^2), \quad \text{for} \quad 0 \leqslant \lambda \leqslant 1, \tag{64}$$

where $\sigma_{\max}$ is the maximum strength of the interface and α a constant used to model the shearing traction more accurately. Note that total debonding occurs when $\lambda = 1$.

This interface model is included as part of an overall surface contact algorithm through the use of interface elements having nodal equivalent forces given by the above defined tractions. Two possibilities need to be considered in the calculation of nodal equivalent forces. The first is the case of separation, $u_n \geqslant 0$, where the two surfaces are pulling away from each other. In this case, the interface law described above is used to apply the appropriate equivalent nodal forces obtained by integration of the traction vector. If interface failure is detected, $\lambda = 1$, the surfaces can separate freely. The second case is that of penetration, $u_n \leqslant 0$. In this case, the contact algorithm provides the equivalent normal nodal forces, while the interface law provides the equivalent nodal tangential forces. Upon interface failure, equivalent nodal tangential forces are computed from the friction law defined previously.

4. Thermal effects

As stated in the introduction, large plastic strains and strain rates result in temperature increases in the body. Hence a temperature-dependent material model and heat conduction need to be added to account for the fact that the behavior of most materials can change dramatically as the temperature rises. The rise in temperature is usually caused by the generation of heat through plastic deformation but can also be the result of friction between sliding interfaces. In this section, a discretized heat equation and its temporal integration is discussed. Moreover, an algorithm accounting for thermal conductance between bodies in contact, *consistent* with the previously presented treatment of mechanical contact, is introduced.

4.1. Governing equations for thermal effects

In a temperature dependent model, an extra level of complexity is added to the governing equations. Heat production and transfer is controlled by the following partial differential equation:

$$k \underbrace{(T_{,xx} + T_{,yy})}_{\nabla^2 T} + Q = c\rho\dot{T}$$

in volume B_t, where heat is generated and transferred. In the above equation, Q is the heat source, ρ the mass density, c the specific heat, and k the thermal conductivity.

Boundary conditions consist of surface prescribed heat flux q_B on surface S_q, prescribed heat convection $h(T_f - T)$ on surface S_c, and a prescribed temperature on surface S_T. These conditions are given for each surface as

$$T = T_B \quad \text{on} \quad S_T, \tag{66}$$

$$q = q_B = k(T_{,x}n_x + T_{,y}n_y) \quad \text{on} \quad S_q, \tag{67}$$

$$q = h(T_f - T) = k(T_{,x}n_x + T_{,y}n_y) \quad \text{on} \quad S_c, \tag{68}$$

where $S = S_T \cup S_c \cup S_q$, h is the heat transfer coefficient, T_f the temperature at infinity, T the temperature on S_c, and $\mathbf{n} = (n_x, n_y)$ the surface normal vector. A weak form of Eqs. (66)–(68) is given by

$$\int_{B_t} (k\nabla^2 T + Q - c\rho\dot{T})\eta \, \mathrm{d}B - \int_{S_q} (k\nabla T \cdot \mathbf{n} - q_B)\eta \, \mathrm{d}S - \int_{S_c} (k\nabla T \cdot \mathbf{n} - h(T_f - T))\eta \, \mathrm{d}S = 0, \tag{69}$$

where η is a test function satisfying the boundary condition $\eta = 0$ on S_T. It can be shown that an equivalent expression of the weak form is

$$\int_{B_t} k(\nabla T \cdot \nabla \eta)\ \mathrm{d}B + \int_{S_c} hT\eta\ \mathrm{d}S + \int_{B_t} c\rho \dot{T}\eta\ \mathrm{d}B = \int_{S_q} q_B \eta\ \mathrm{d}S + \int_{B_t} Q\eta\ \mathrm{d}B + \int_{S_c} hT_f \eta\ \mathrm{d}S. \tag{70}$$

This equation expresses an energy balance wherein the change in heat energy in volume B_t is equal to the net heat added.

For a finite element approach, a Galerkin method provides the discretization

$$\mathbf{T}(\mathbf{x}) = \mathbf{N}(\mathbf{x})\mathbf{T}_e, \tag{71}$$

$$\eta(\mathbf{x}) = \mathbf{N}(\mathbf{x})\eta_e, \tag{72}$$

$$\mathbf{T}_\partial = \mathbf{B}\mathbf{T}_e, \tag{73}$$

in which $\eta(\mathbf{x})$ is a weight function approximated using the same shape functions $\mathbf{N}$ as used for T. Note that these shape functions are defined in the deformed configuration. The quantity $\mathbf{T}_e$ is the array of nodal temperatures for an element, while $\mathbf{T}_\partial$ is the matrix containing the partial derivatives of T_e across the element.

Given the above spatial discretization, the governing equations simplify to a first order set of ordinary differential equations, viz.,

$$(\mathbf{K} + \mathbf{H})\mathbf{T} + \mathbf{C}\dot{\mathbf{T}} = \mathbf{R}_q + \mathbf{R}_Q + \mathbf{R}_h, \tag{74}$$

wherein the global characteristic conduction, convection, and rate dependent matrices $\mathbf{K}$, $\mathbf{H}$, $\mathbf{C}$ determine the response of the system. They may be compiled from the element matrices by

$$\mathbf{K} = \sum_e \mathbf{k}_e = \sum_e \int_{A_e} \mathbf{B}^{\mathrm{T}}\mathbf{k}\mathbf{B}\ \mathrm{d}A, \tag{75}$$

$$\mathbf{H} = \sum_e \mathbf{h}_e = \sum_e \int_{S_c} \mathbf{N}^{\mathrm{T}} h \mathbf{N}\ \mathrm{d}S, \tag{76}$$

$$\mathbf{C} = \sum_e \mathbf{c}_e = \sum_e \int_{A_e} \mathbf{N}^{\mathrm{T}} \rho c \mathbf{N}\ \mathrm{d}A. \tag{77}$$

The thermal load vectors are given by

$$\mathbf{R}_q = \sum_e \int_{S_B} \mathbf{N}^{\mathrm{T}} q_B\ \mathrm{d}S, \tag{78}$$

$$\mathbf{R}_h = \sum_e \int_{S_c} \mathbf{N}^{\mathrm{T}} T_f h\ \mathrm{d}S, \tag{79}$$

$$\mathbf{R}_Q = \sum_e \int_{A_e} \mathbf{N}^{\mathrm{T}} Q\ \mathrm{d}A, \tag{80}$$

where $\mathbf{R}_q$, $\mathbf{R}_h$, and $\mathbf{R}_Q$ are the thermal load vectors.

If thermal conductivity is assumed to be a crystal property, then the large displacements and rotations introduced by the elastic part of the deformation gradient needs to be accounted for. Following Lubliner (1990), we define $\mathbf{k} = k\mathbf{F}^e\mathbf{F}^{eT}$ in Eq. (75). Furthermore, for the plastic process defined earlier, a heat supply Q due to the rate of plastic work, $\dot{W}^p$, can be estimated by the Taylor–Quinny formula, viz.,

$$Q = \delta \dot{W}^p, \tag{81}$$

in which δ is a coefficient of the order of 0.8–0.9.

The whole system of equations may be simplified by joining $(\mathbf{K} + \mathbf{H}) = \hat{\mathbf{K}}$, so that

$$\hat{\mathbf{K}}\mathbf{T} + \mathbf{C}\dot{\mathbf{T}} = \mathbf{R}. \tag{82}$$

Now, using a direct integration method, the temperature field is computed at each time step as

$$\left(\frac{1}{\Delta t}\mathbf{C} + \beta\hat{\mathbf{K}}\right)\mathbf{T}_{n+1} = \left(\frac{1}{\Delta t}\mathbf{C} - (1-\beta)\hat{\mathbf{K}}\right)\mathbf{T}_n + (1-\beta)\mathbf{R}_n + \beta\mathbf{R}_{n+1} \tag{83}$$

so that, if $\beta = 0$, the process becomes an explicit integration algorithm, namely,

$$\mathbf{C}\mathbf{T}_{n+1} = (\mathbf{C} - \Delta t\hat{\mathbf{K}})\mathbf{T}_n + \mathbf{R}_n. \tag{84}$$

This assumes, of course, initial conditions $\mathbf{T} = \mathbf{T}_0$ at $t = 0$, as well as a time step below $\Delta t_{\mathrm{cr}} = 2/(1-2\beta)\lambda_{\max}$, where $\lambda_{\max}$ is the maximum eigenvalue associate to the first order system of ordinary differential equations. In addition, if $\mathbf{C}$ is lumped the algorithm does not require factorization of $\mathbf{C}$ in the determination of $\mathbf{T}_{n+1}$.

4.2. Thermal contact conductance

In many problemas involving interfacial sliding, a formulation accounting for heat fluxes between solid bodies is needed. In this section we derive such a scheme *consistently* with the treatment of

mechanical contact, i.e., we define master and slave surfaces each having a different temperature. If the mechanical contact determines penetration, we define a heat flux between the surfaces due to a temperature jump and heat generated at the frictional contact resulting from a jump in velocities across the sliding surface. This heat flux is given by

$$q_p = \beta[h_s(T_s - T_m) - \mathbf{t}\cdot(\mathbf{v}_s - \mathbf{v}_m)], \tag{85}$$

in which $\mathbf{t}$ is the contact traction vector, $\mathbf{v}_s$ and $\mathbf{v}_m$ are the slave and master nodal velocity vectors, T_s is the temperature of the slave node and T_m is the temperature of the master surface at the projection point, viz.,

$$T_m = \xi T_2 + (1-\xi)T_1, \tag{86}$$

where T_1 and T_2 are the temperatures of the precedent and antecedent nodes, respectively, on the master segment. The contact heat transfer coefficient h_s, introduced in Eq. (85), is a function of surface roughness L_g, contact area fraction f_c, material conductivity of the slave and master surfaces k_s and k_m, the conductivity of the material filling the interface k_f, and void area fraction f_v, Özisik (1977),

$$h_s = \frac{1}{L_g}\left(f_c\frac{2k_sk_m}{k_s+k_m} + f_vk_f\right). \tag{87}$$

In general $k_f \ll k_s, k_m$ so the last term in the above equation can be neglected. The contact area fraction generally depends on interface pressure. We propose to use an exponential law for f_c given by

$$f_c = 1 - c_1\mathrm{e}^{-c_2p}, \tag{88}$$

where c_1 and c_2 are parameters defining the initial area fraction and the rate at which f_c approaches unity with pressure.

The heat flux, defined in Eq. (85), is distributed in both surfaces consistently with the discretized formulation of the heat equation. Equivalent nodal forcing terms are computed by

$$\mathbf{r}_q^s = \int_{A_s}\mathbf{N}^{\mathrm{T}}q_p\,\mathrm{d}A, \tag{89}$$

where A_s is the slave node influence surface area. This force is balanced to the master nodes using the variable ξ, distance from the first node of the contact face to the projection point, nondimensionalized by the length of the face,

$$\mathbf{r}_{q1}^s = (1-\xi)\mathbf{r}_q^s, \tag{90}$$

$$\mathbf{r}_{q2}^s = \xi\mathbf{r}_q^s. \tag{91}$$

For a time increment Δt, slave and master nodes temperatures are corrected according to the following expressions,

$$c_{s1} = (1-\xi)c_s, \tag{92}$$

$$c_{s2} = \xi c_s, \tag{93}$$

$$\left(c_I + \sum_s c_{sI}\right)\Delta T_I = \sum_s \mathbf{r}_{qI}^s\Delta t, \tag{94}$$

$$T_I = \hat{T}_I + \Delta T_I, \tag{95}$$

$$\Delta T_s = (1-\xi)\Delta T_1 + \xi\Delta T_2, \tag{96}$$

$$T_s = \hat{T}_s + \left(\Delta T_s - \frac{r_q^s\Delta t}{c_s}\right). \tag{97}$$

In the above equations, the summation is over the contributions from the slave nodes contacting master node I, and ΔT_s and ΔT_I are predicted temperatures in the absence of heat conduction at the contact surfaces. It should be noted that, in contrast to the work by Marusich and Ortiz (1995), in the present algorithm no assumption implying continuity of the temperature field across the contact surface is made. Moreover, thermal contact conductance and frictional heat sources are naturally incorporated in the mechanical contact algorithm. The scheme is easily implemented as part of the contact algorithm discussed previously.

5. Adaptive mesh refinement

Element distortion in Lagrangian dynamic finite element calculations can reduce the stable time step of an explicit time integrator to a point where the computation no longer advances and the field variables are not accurately interpolated. A solution to this problem is to rediscretize the domain with a new, undistorted mesh, and continue with the calculation. In history dependent problems,

as the mesh is adapted, the solution cannot be computed from the initial state but has to be continued from the previously computed state. This requires a procedure to transfer the problem state variables from the old mesh M_n to the new mesh M_{n+1}, while satisfying the field and constitutive equations, such that the calculation may continue without excessive error. The *transfer operator* needs to address the following issues.

(i) Requirements of static or dynamic equilibrium.
(ii) Consistency with the constitutive equations.
(iii) Compatibility of the state transfer with the displacement field on the new mesh M_{n+1}.
(iv) Compatibility with evolving boundary conditions.
(v) Minimization of numerical diffusion of state variables.

5.1. Update of configuration

Central to the idea of replacing an old, highly distorted mesh, with a new, undeformed mesh is the update of the reference configuration. The model presented earlier, governing the body behavior, uses a Lagrangian formulation. If a mesh is rebuilt, but the reference configuration is *not* updated, the distortion merely changes its location from the current configuration to that of the reference. To truly remove the distortion, the reference configuration must be perodically moved forward to the current configuration.

The reference configuration is defined as the configuration at which the displacements are zero. So part of updating the reference configuration is setting

$$\hat{\mathbf{x}} = \mathbf{X} + \mathbf{u}, \tag{98}$$

$$\hat{\mathbf{u}} = \mathbf{0}, \tag{99}$$

$$\mathbf{x} = \hat{\mathbf{x}} + \hat{\mathbf{u}}, \tag{100}$$

wherein $\mathbf{X}$, $\mathbf{u}$, $\hat{\mathbf{x}}$, and $\hat{\mathbf{u}}$ are the reference particle positions and displacements in the old and new reference configurations, respectively. In addition, after the update, the new current particle position $\mathbf{x}$ is defined by the new reference $\hat{\mathbf{x}}$ and displacement $\hat{\mathbf{u}}$, as depicted in Fig. 7. More is required, however. Remember that the deformation gradient relates the current configuration to the reference configuration by

$$\mathbf{F} = \frac{\partial \mathbf{x}}{\partial \mathbf{X}} = \frac{\partial(\mathbf{X} + \mathbf{u})}{\partial \mathbf{X}} = \mathbf{I} + \frac{\partial \mathbf{u}}{\partial \mathbf{X}}, \tag{101}$$

where $\mathbf{x}$ is the current position field. When the reference configuration is updated, however, the rela-

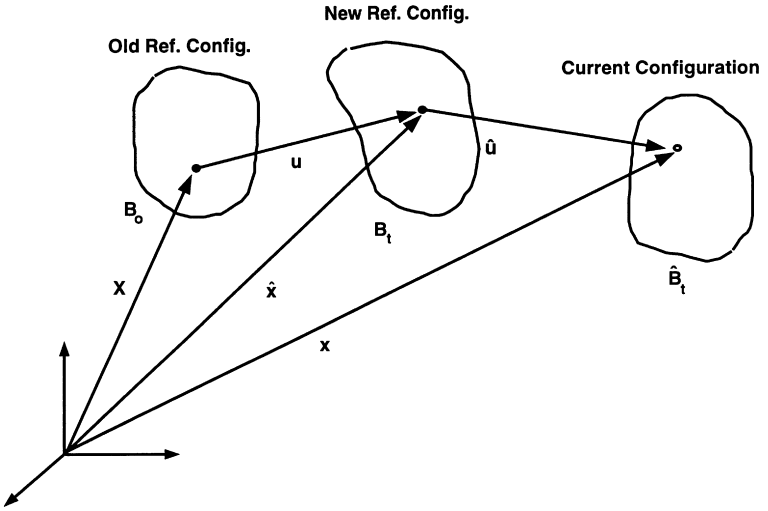

Fig. 7. Update of current configuration.

tion becomes a bit more complicated. After an update, the deformation gradient expands to

$$\mathbf{F} = \frac{\partial \mathbf{x}}{\partial \mathbf{X}} = \frac{\partial(\mathbf{X} + \mathbf{u} + \hat{\mathbf{u}})}{\partial \mathbf{X}} \tag{102}$$

$$= \mathbf{I} + \frac{\partial \mathbf{u}}{\partial \mathbf{X}} + \frac{\partial \hat{\mathbf{u}}}{\partial \hat{\mathbf{x}}}\frac{\partial \hat{\mathbf{x}}}{\partial \mathbf{X}} \tag{103}$$

$$= (\mathbf{I} + \frac{\partial \mathbf{u}}{\partial \mathbf{X}}) + \frac{\partial \hat{\mathbf{u}}}{\partial \hat{\mathbf{x}}}(\mathbf{I} + \frac{\partial \mathbf{u}}{\partial \mathbf{X}}) \tag{104}$$

such that $\partial \mathbf{u}/\partial \mathbf{X}$ may be stored and reset at each update as

$$\frac{\partial \mathbf{u}}{\partial \mathbf{X}} = \mathbf{F} - \mathbf{I}. \tag{105}$$

We can then compute the deformation gradient $\mathbf{F}$ as

$$\mathbf{F}^{\text{old}} = \mathbf{I} + \frac{\partial \mathbf{u}}{\partial \mathbf{X}}, \tag{106}$$

$$\mathbf{F} = \mathbf{F}^{\text{old}} + \frac{\partial \hat{\mathbf{u}}}{\partial \hat{\mathbf{x}}}(\mathbf{I} + \frac{\partial \mathbf{u}}{\partial \mathbf{X}}). \tag{107}$$

In discretized form, Eq. (104) becomes

$$F_{iJ} = \sum_{a=1}^{\text{NEN}} N_{a,J} x_{ia} \tag{108}$$

$$= I_{iJ} + \sum_{a=1}^{\text{NEN}} N_{a,J} u_{ia} + \sum_{a=1}^{\text{NEN}} \hat{N}_{a,k}\hat{u}_{ia}(I_{kJ} + \sum_{b=1}^{\text{NEN}} N_{b,J} u_{kb}), \tag{109}$$

where NEN is the number of nodes per element. Shape functions derivatives, $N_{a,J}$ and $\hat{N}_{a,k}$, are defined with respect to the original and new reference configurations, respectively.

5.2. Transfer of variables

Transfer of state variables can be accomplished mainly in two ways.

(i) Direct transfer from Gauss points of the old mesh M_n to the new mesh M_{n+1} by standard interpolation,

(ii) Construct a solution which is continuous by a suitable projection of state variables at quadrature points, Zienkiewicz and Taylor (1991a), namely,

$$\int_{\Omega} P[Q^*_{n+1} - Q_{n+1}]d\Omega = 0 \tag{110}$$

where P is a suitable projection operator, Q^*_{n+1} are the projected state variables, and Q_{n+1} are the state variables obtained from the finite element solution.

A typical projections is obtained by using as P the element shape functions. Depending on the domain Ω used in the projection, a local or global transfer is obtained. This projection works very well for the calculation of nodal stresses, but can lead to *numerical diffusion* of internal variables in regions of sharp gradients. Practice shows that numerical diffusion is less pronounced when direct transfer from the Gauss points of the old mesh to the Gauss points of the new mesh is performed.

5.2.1. Interpolation and consistent computation of field variables

In this subsection, a mesh transfer operator for 6-noded triangular elements, with full integration, is described. These elements are selected because construction of meshes by triangulation can be done simply and automatically. Furthermore, it is known that first order triangles suffer from volumetric and shear locking (Nagtegaal et al., 1974). By contrast, six-noded elements with linear strain interpolation do not lock (Hughes, 1987).

State variables in the new mesh are subdivided in two sets, interpolated and computed variables, see Table 3. For the interpolated set, the state variables are interpolated in the deformed configuration based upon shape functions of an auxiliary element connectivity of simple 3-node triangles connecting all of the existing nodes in the old mesh M_n. For each node in the new mesh, the area coordinates of that node are computed for each auxiliary element connecting nodes in the old mesh. These area coordinates are then used as shape functions for the interpolation of the nodal variables. This sort of interpolation is conducted for the nodal kinematic quantities, including displacement, velocity, and acceleration. In addition, the same sort of interpolation is performed for the components of the stress tensor $\overline{\mathbf{S}}$ and the internal variables $\overline{\mathbf{Q}}$ using this time an auxiliary mesh

Table 3
Interpolated and computed state variables

Set of interpolated variables: $\mathbf{I}(\mathbf{u}, \mathbf{v}, \mathbf{a}, T, \overline{\mathbf{S}}, \epsilon^p, \hat{\boldsymbol{\epsilon}}^p, \theta, \mathbf{F}^{\text{old}})$
Set of computed variables: $\mathbf{C}(s, \overline{\mathbf{C}}^e, \mathbf{F}^e, \mathbf{F}^p)$

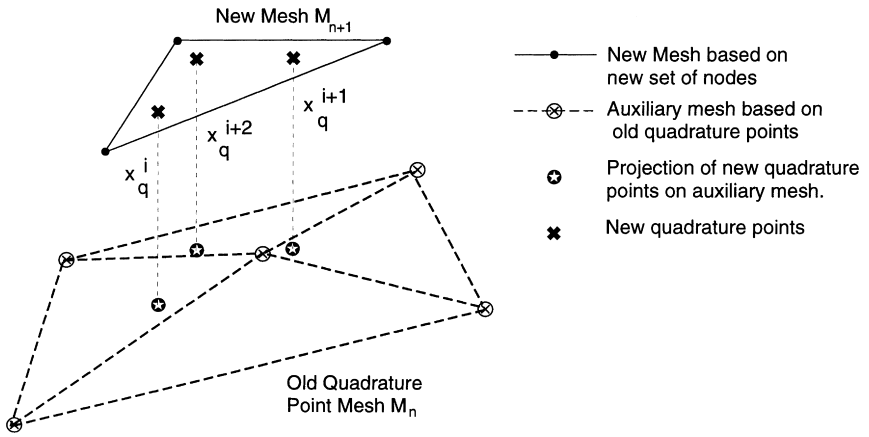

Fig. 8. Interpolation from quadrature points in the old mesh to quadrature points in the new mesh.

obtained by 3-node triangular elements connecting quadrature points in the old mesh, as shown in Fig. 8.

It should be noted that not all of the variables may be interpolated. If everything was interpolated, the stress state after the mesh update would be inconsistent with the state of displacement. The problem then requires a suitable choice of field variables to be interpolated and other field variables to be computed to keep the solution stable and consistent with the equations of motion and the material constitutive equations. The field variables are divided into an interpolated set **I** and a computed set **C**. The choice of interpolating $\overline{\mathbf{S}}$ instead of $\mathbf{F}^p$, is based on the fact that errors produced in the interpolation of $\mathbf{F}^p$ are amplified by the elastic moduli in the computation of stress from $\mathbf{F}^e = \mathbf{F}\mathbf{F}^{p^{-1}}$. This is possibly the most important choice of our remeshing scheme and differentiates it from other transfer operators proposed in the literature, e.g., Marusich and Ortiz (1995). Remember that the deformation gradient has the multiplicative decomposition $\mathbf{F} = \mathbf{F}^e\mathbf{F}^p$. Hence, after interpolation of the set **I** the $\mathbf{F}^p$ can be computed from the stresses and displacements so that any error introduced through the remeshing is minimized and ends up in a compatible $\mathbf{F}^p$.

The calculation of $\mathbf{F}^p$ requires the determination of the elastic part of the deformation gradient in the old mesh. Since in our finite deformation elasticity law, $\overline{\mathbf{S}} = L0.5\ \ln\ \overline{\mathbf{C}}^e$, where $\overline{\mathbf{C}}^e = \mathbf{F}^{e\mathrm{T}}\mathbf{F}^e$, the rotation tensor $\mathbf{R}^e$ needs to be transferred between the new and old meshes to allow the calculation of $\mathbf{F}^e$ from $\overline{\mathbf{S}}$. Therefore, before the interpolation is begun, the deformation gradient **F** is computed from the displacement field and the elastic part of **F**, $\mathbf{F}^e$, is computed from the multiplicative decomposition of **F** at the quadrature points in the old mesh, namely,

$$\mathbf{F}^e = \mathbf{F}\mathbf{F}^{p^{-1}}. \tag{111}$$

Then, through a polar decomposition of $\mathbf{F}^e$, a rotation matrix $\mathbf{R}^e$ may be identified, and rendered down to a rotation angle θ as shown below.

$$\mathbf{R}^e = \mathbf{F}^e\mathbf{U}^{e-1},$$

$$\mathbf{R}^e = \begin{pmatrix} \cos\ \theta & -\sin\ \theta & 0 \\ \sin\ \theta & \cos\ \theta & 0 \\ 0 & 0 & 1 \end{pmatrix}. \tag{112}$$

This theta is interpolated with the internal variables, then used to rebuild $\mathbf{R}^e$ for the subsequesnt calculation of $\mathbf{F}^p$ in the new mesh. Once the stresses and rotation angle have been interpolated, the shape functions in the new mesh calculated, and the deformation gradient **F** computed, from the interpolated displacement field **u** and $\mathbf{F}^{\mathrm{old}}$, in the new mesh M_{n+1}, the plastic part of the deformation gradient $\mathbf{F}^p$ is recalculated for each quadrature point in M_{n+1}.

In order to preserve the strain rate and ensure the plastic deformation is isochoric, corrections

need to be carried on in the interpolated second Piola–Kirchhoff stress tensor $\overline{\mathbf{S}}$ and the computed $\mathbf{F}^e$ as described below. Before calculating $\mathbf{F}^e$, the interpolated stresses must be corrected to maintain a consistent rate of plastic straining. The current material strength $s(\epsilon^p, T)$ is updated using the interpolated effective plastic strain ϵ^p according to Eq. (23). In addition, the deviatoric portion of the second Piola-Kirchhoff stress tensor, $\overline{\mathbf{S}}_{\text{dev}}$, of the interpolated stress tensor is corrected using an interpolated effective plastic strain rate $\dot{\epsilon}^p$, viz.,

$$\overline{\mathbf{S}}_{\text{dev}}^{\text{corr}} = \overline{\mathbf{S}}_{\text{dev}}^{\text{int}} \frac{\mathbf{s}}{\overline{\sigma}} \left(\frac{\dot{\epsilon}^p + \dot{\epsilon}_o^p}{\dot{\epsilon}_o^p} \right)^{1/\alpha}, \tag{113}$$

after which the stress tensor is rebuilt with the new $\mathbf{S}_{\text{dev}}$. This is done to preserve the plastic strain rate through the mesh, as the plastic strain rate is sensitive to sudden changes in the effective stress. The elastic right Cauchy–Green deformation tensor is reconstructed from the material stiffness tensor L and the second Piola–Kirchhoff stress $\overline{\mathbf{S}}$, to produce the elastic part of the deformation gradient $\mathbf{F}^e$, namely,

$$\mathbf{C}^e = \exp(2L^{-1}\overline{\mathbf{S}}), \tag{114}$$

$$\mathbf{F}^e = \mathbf{R}^e \sqrt{\mathbf{C}^e}. \tag{115}$$

Before computing $\mathbf{F}^p$, $\mathbf{F}^e$ is scaled so that $\det \mathbf{F}^e = \det \mathbf{F}$. This is necessary because the plastic deformation is assumed to be isochoric ($\det \mathbf{F}^p = 1$). Finally, the plastic deformation gradient is computed by

$$\mathbf{F}^p = \mathbf{F}^{e^{-1}} \mathbf{F}. \tag{116}$$

If everything is done correctly, the $\mathbf{F}^p$ after remeshing should resemble the $\mathbf{F}^p$ in the old mesh. A summary of our mesh transfer algorithm is given in Tables 4 and 5.

Table 4
Flowchart for the calculation of variables in set **C** from the interpolated set **I**

$$\mathbf{u} \rightarrow \mathbf{F} \rightarrow \mathbf{F}_{\text{corr}} = \left(\frac{\det \mathbf{F}^e}{\det \mathbf{F}} \right)^{1/3} \mathbf{F}$$

$$\downarrow$$

$$\mathbf{F} = \mathbf{F}^e \mathbf{F}^p \rightarrow \mathbf{F}^p = \mathbf{F}^{e^{-1}} \mathbf{F}$$

$$\uparrow$$

$$\theta \rightarrow \mathbf{R}^e \sqrt{\overline{\mathbf{C}}^e} = \mathbf{F}^e \rightarrow \det \mathbf{F}^e$$

$$\uparrow$$

$$\overline{\mathbf{C}}^e = \exp(2\mathbf{L}^{-1}\overline{\mathbf{S}})$$

$$\uparrow$$

$$\dot{\epsilon}^p, \overline{\mathbf{S}} \rightarrow \overline{\mathbf{S}}_{\text{dev}}^{\text{corr}} = \mathbf{S}_{\text{dev}}^{\text{int}} \frac{s}{\overline{\sigma}} \left(\frac{\dot{\epsilon}^p + \dot{\epsilon}_0^p}{\dot{\epsilon}_0^p} \right)^{1/\alpha}$$

$$\uparrow$$

$$\dot{\epsilon}^p, \overline{\mathbf{S}} \rightarrow s = \sigma_0 \left(1 + \frac{\epsilon^p}{\epsilon_0^p} \right)^{1/\beta} \left[1 - \left(\frac{T - T_0}{T_m - T_0} \right)^{\gamma} \right]$$

Table 5
Field variables transfer algorithm

1. Define boundaries for new mesh based on old mesh.
2. Create new set of corner nodes from old mesh. Refine as necessary.
3. Create new elements by Delaunay triangulation.
4. Remove elements created outside mesh boundaries.
5. Optimize element shapes.
6. Define auxiliary interpolation meshes connecting nodes, quadrature points.
7. Perform polar decomposition on $\mathbf{F}^e$, and save orientation in θ.
8. Interpolate variables in set **I** (see Table 3).
9. Update reference configuration.
10. Compute new shape functions.
11. Compute variables in set **C** (see Table 3).
12. Replace old state variables with new, and continue with the calculation.

5.3. Remeshing and mesh refinement method

5.3.1. Remeshing condition

Transferring the state of a calculation from one discretization to another is computationally expensive. The key, therefore, to decide when to undergo this process must be based on error estimates or in the case of explicit time integrators, when the stable time step decreases to point that advances in time fall below a prescribed value. A simple criterion for remeshing, therefore, is to set a threshold time step that will force remeshing. The condition

currently in use compares the current time step to a reference value set at the end of the previous remeshing. In this way, if the time step dwindles to below a fraction of its reference value, a remeshing will be triggered. This fraction is provided by the user.

5.3.2. Refinement condition

When remeshing, it is useful to introduce more elements in those regions of the mesh that are rapidly deforming. One way of deciding which regions need to be refined is to examine the rates of plastic work being produced in the elements, temperature rise, the second invariant of the deviatoric rate of deformation tensor, the maximum principal strain, or the equivalent strain (Batra and Kuo, 1992; Batra and Hwang, 1993). All these measures become quite large in regions where the material is deforming inelastically at a high rate, for instance within shear bands.

In the example later presented, the rate of plastic work $\dot{W}^p$ is computed at each quadrature point as $\dot{W}^p = \overline{\sigma}\dot{\epsilon}^p$. These work rates are averaged for the element. The element rates are in turn averaged over the whole mesh. Each element rate is compared to the average to decide whether the element should be refined, coarsened, or left unchanged. This is made dependent on user-supplied thresholds, as in

$$I_e = \sum_{i=1}^{\mathrm{NQUAD}} \dot{W}_i^p/\mathrm{NQUAD}, \tag{117}$$

$$I = \sum_{e=1}^{\mathrm{NUMEL}} I_e/\mathrm{NUMEL}, \tag{118}$$

$$\beta_e = I_e/I, \tag{119}$$

$$\begin{array}{ll} \beta_e > \beta_{\max} & \text{needs to refine,} \\ \beta_e < \beta_{\min} & \text{needs to coarsen,} \end{array} \tag{120}$$

where $\beta_{\max}$ is a threshold number greater than one, and $\beta_{\min}$ is between zero and one. In addition, maximum and minimum element sizes are defined to limit refinement and coarsening that could lead to excessive computational times or poor accuracy.

5.3.3. Element refinement

When a remeshing is triggered, the new mesh is created by a delaunay triangulation algorithm, redefining the element connectivity using the current locations of all of the corner nodes from the old mesh. When an element is flagged for refinement, its midnodes are added to the corner node list, resulting in several elements being created where just one existed before. This method for refinement is used primarily because it is a very simple and easy way to introduce new elements. Even those elements which are not refined or optimized are improved in the remeshing operation. As the delaunay triangulation routine creates new 6-node elements from existing corner nodes, it attempts to connect them so that the elements are as close to equilateral as convenient. In addition, new midnodes are created at the midpoints of the element sides, so that new elements are perfectly triangular. Of course, mesh refinement requires several other considerations that greatly depend on the specifics of the problem being studied. For example, the boundary conditions would need to be set for the new mesh and the nodes on the surfaces of bodies redefined for contact. In addition, in a multi-body contact problem, it is possible that for some of the bodies, remeshing is neither needed nor desired. These are problems that may be considered on a case-by-case basis.

5.4. Mesh optimization

Not all meshes are suitable for finite element calculations. The error due to the approximations depends on the size and the shape of the elements. The element sizes are chosen as a compromise between accuracy and computing cost, and may vary through the domain according to error estimates or user's experience. Good meshes may be set apart from bad ones by the shapes of the elements contained within. Distorted elements produce errors which degrade the quality of the calculation, and elements with a good initial shape may distort as they follow the movement of the domain's boundary. This has motivated intensive research on mesh-improving techniques, and much experience in smoothing meshes has come from the field of deformable domains. In Zavattieri et al. (submitted), it was proposed to use, as quality of the mesh, the quality of its *worst* element, defined by a measure Q,

$$Q_{\text{global}} = \min_k Q_k. \tag{121}$$

This choice incorporates a well-known fact that one unacceptable element renders the mesh useless. The problem then becomes one of maximizing an objective function of the min type. As min functions are nondifferentiable, a simple node-by-node algorithm (described later) is used. This implementation uses a node-movement algorithm that, in most cases, produces a sequence of meshes of nondecreasing quality.

5.4.1. A global mesh optimization algorithm

The simultaneous optimization of the locations of all of the nodes in a mesh consisting of thousands of elements is obviously untractable. In Zavattieri et al. (submitted), it is shown that to improve the worst element of the mesh, it is only necessary to move those nodes located in close vicinity to it (up to its neighbors of order 1 or 2). Also, in Zavattieri et al. (1996), they have incorporated a computationally inexpensive measure of the quality of a triangle, namely,

$$Q_e = C\frac{A_e}{\mathscr{P}_e^2}, \tag{122}$$

where A_e is the area of element e, $\mathscr{P}_e$ its perimeter (the sum of the lengths of its three edges), and C is a constant which renders the quality of an equilateral triangle equal to one ($C = 20.784619$). The advantages of this definition of quality is discussed in Zavattieri (1995).

The objective function Q_{global} is maximized over the space of nodal locations. We only modify the positions of those nodes that belong to the worst element of the mesh, and their nth-order neighbors (with $n = 1$ or 2). We will refer to as *moving nodes* those nodes that are moving at a given stage of the algorithm. The *moving nodes* are selected among the *movable nodes*. In the present version of our method, boundary nodes are *nonmovable*. If all the nodes belonging to an element are *nonmovable*, the element is not considered. The algorithm which identifies nodes as *moving*, *movable* or *nonmovable* is displayed in Table 6. The current implementation uses NL = 2, and $M = \text{NUMEL}/3$ where NUMEL is the number of element of the mesh.

5.4.2. Local cluster optimization

The nodal position of each node I is modified to maximize the quality Q_e of the elements that share this node. Let us define the *cluster* C_I associated to a node I of a triangulation as the set of elements that share this node. We associate to the cluster C_I a scalar quantity, the quality of the cluster, defined by

$$q_C = \min_{e \in C_I} Q_e. \tag{123}$$

Quality q_C is continuous function of the position x_I of the central node I of the cluster. We next introduce a set of sampling positions. Let x_I^0 be the original position of node I. Then, for every vertex V of the cluster define two sampling points located at

$$x_{sp} = \pm\alpha x_v + (1 \mp \alpha)x_I^0, \tag{124}$$

where α is a small parameter, typically 0.05. Notice that x_I^0 is itself a sampling position. In two dimensions, the set of sampling points defined in this way would look much as in Fig. 9.

Table 6
Identification of moving nodes

1. Initialization and Global Parameters: Specify a neighborhood level NL and a maximum number of iterations M. Set boundary nodes as nonmovable. Initialize an integer auxiliary constant PREV with 0.
2. Identify the worst element among those elements of the mesh containing at least one *movable node*, KWORST. If the number of *movable nodes* is zero, stop.
3. If KWORST = PREV, set the three corner nodes of KWORST as *nonmovable* and go back to 2.
4. Identify the nodes in a neighborhood of order NL of KWORST. The neighbors of order 0 are the four nodes belonging to KWORST. Neighbors of order 1 are those nodes that are not neighbors of order 0, but are connected by an edge with at least one neighbor of order 0; and so on.
5. Set as *moving nodes* those identified in 3 that have not previously been set as *nonmovable*. Sweep these *moving nodes* modifying the nodal positions one at a time, according to the *local cluster optimization* rule, so as to improve the quality of the cluster.
6. Assign to PREV the value KWORST.
7. Go back to 2, or Stop if the number of iterations is equal to M.

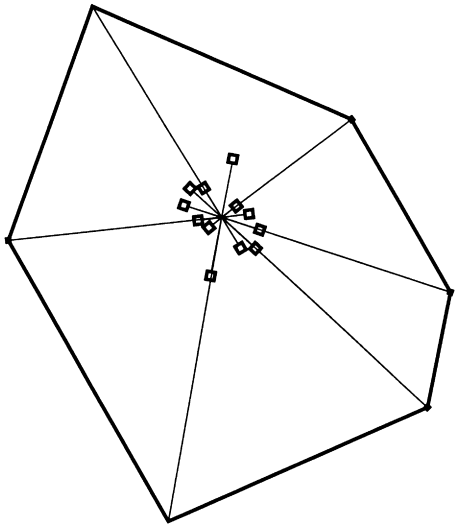

Fig. 9. Sampling positions for local cluster optimization in 2-D.

The local cluster optimization rule that has been implemented is the following:

Evaluate q_I for all sampling positions, and choose as updated position the sampling position that maximizes this quality.

Most clusters with bad initial quality attain very high quality in just a few iterations, and then spend lots of local iterations improving the quality from, say, 0.4–0.45. A good implementation should consider this possibility and stop the local iterations whenever a cluster has reached a quality that is greater that some given threshold value QTol, so as to avoid wasting CPU time improving already-good clusters, and turn to worse ones. In the calculations later reported a value of $Q\text{Tol} = 0.9$ was used.

6. An application to rod on rod impact

One important objective in developing a finite element model accounting for large deformation plasticity and brittle failure is the ability of simulating specially designed experiments towards the identification of material inelasticity and failure mechanisms. One such experiment involves the collision of a 6061-T6 aluminum anvil with unconfined and confined AD-99.5 alumina rods in a modified Taylor test (Wise and Grady, 1994). In this test, interferometric measurement of radial and axial velocities provides an estimate of the compressive dynamic yield strength of the ceramic rod under uniaxial stress. In Wise and Grady experiments, the ceramic rod free end velocity was measured with a velocity interferometer (VISAR). Unlike the Taylor test, which was extensively used in the high strain rate characterization of metals, analyses of the experimentally recorded velocity histories do not rely on any simplifying assumptions regarding rod deformation, and do not require an intact rod for recovery. This makes the modified Taylor test very useful for the study of ceramics failure through numerical simulation of the failure event.

6.1. Problem geometry

For this problem, the aluminum impactor is formed into a 134.7 mm long T-shaped rod with diameters of 20 and 89 mm for the rod and T-flange, respectively. The flange is 12.7 mm thick, while the trailing rod is 122 mm long. The rod section of the anvil was initially incorporated by Wise and Grady to maximize the duration of high stress levels at the impact end of the target rod. The ceramic rod being tested is an AD-99.5 alumina rod 80 mm long, with a 10.06 mm diameter. In the case of confined alumina, a tantalum sleeve, 20 mm in diameter, is used.

In our simulations, the anvil is modeled with 6-node axisymmetric triangular elements using the large deformation plasticity model presented earlier. Mesh refinement and optimization are performed. The ceramic rod also uses 6-node axisymmetric triangular elements, but this time based on the small-strain microcracking multiple-plane model previously discussed. No remeshing or optimization is done for the alumina rod. Since material models for fragmentation of ceramics accounting for temperature effects are not currently available, we have not computed the thermal field. The properties of the two materials being used and the parameters used in the definition of contact are displayed in Tables 7–9. The ceramic model

Table 7
Material properties for aluminum and tantalum

	6061-T6 Aluminum	Tantalum
Elastic properties		
E [GPa]	69.0	189.38
v	0.3299	0.3327
ρ_0 [kg/m^3]	2700	16607
Inelastic properties		
σ_0 [MPa]	270	700
ϵ_0^p	0.003913	0.003696
$\dot{\epsilon}_0^p$ [s^{-1}]	1000	1000
α	3	5
β	15	5

Table 8
Material properties for alumina

AD-99.5 Alumina ceramic	
Elastic properties	
$E = 374$ GPa	Young's modulus
$\mu = 0.22$	Poisson's ratio
$\rho_0 = 3890$ kg/m^3	Density
Inelastic properties	
$v = 0.1$	Internal friction coefficient
$c_R = 5000$ m/s	Wave speed
$K_{IC} = 1.7 \times 10^6$	Critical stress intensity factor
$a_0 = 10$ μm	Initial crack radius
$c_n^1 = 1.0 \times 10^{12}\ m^{-3}$	Crack density for plane 1
$c_n^2 = 1.0 \times 10^{12}\ m^{-3}$	Crack density for plane 2
$c_n^3 = 0.0$	Crack density for plane 3
$c_n^4 = 0.0$	Crack density for plane 4
$c_n^5 = 0.0$	Crack density for plane 5
$c_n^6 = 5.0 \times 10^{10}\ m^{-3}$	Crack density for plane 6
$c_n^7 = 0.0$	Crack density for plane 7
$c_n^8 = 5.0 \times 10^{10}\ m^{-3}$	Crack density for plane 8
$c_n^9 = 0.0$	Crack density for plane 9
$n^+ = 0.3$	Ratio 1 (tension)
$n^- = 0.1$	Ratio 2 (compression)
$m^+ = 0.3$	Power 1 (tension)
$m^- = 0.1$	Power 2 (compression)

Table 9
Contact constants

Contact properties	
$\mu_0 = 0.0$	Static friction coeff.
$\mu_\infty = 0.0$	Dynamic friction coeff.
$\gamma = 0.0$	Friction law exponent
$\beta = 0.0$	Contact weighting parameter

parameters are selected such that a damage threshold is properly captured and at the same time they are in agreement with values reported in the literature. It should be noted that microstructural differences have an effect on model parameters. For instance, the existence of a second phase at the grain boundaries controls parameters μ, $n^{\pm}, m^{\pm}$ and K_{IC}. The grain size controls the values of a_0 and maximum crack density of each orientation. The choice of different crack densities as a function of orientation is motivated by experimental data (Espinosa et al., 1992) indicating that the density of active microcracks is a function of the mechanism responsible for crack nucleation. In the case of predominantly compressive stress states, glass at the grain boundaries determines the early stages of inelasticity and acts as a precursor for the development of triple point microcracks. In the case of predominantly tensile stress states, cracks are mainly nucleated due to grain boundary decohesion at a much lower stress level. In the present axisymmetric calculations, plane 1 is a plane on which positive normal tractions result from unloading waves emanating from the bar surface. By contrast planes 6 and 8 are mainly shear cracks.

In the calculation featured here, the anvil strikes the specimen at 1035 m/s (for confinement 1051 m/s), in an attempt to simulate the conditions for shots 5 and 6 in Wise and Grady's experiments.

6.2. Velocity and stress histories

During the impact calculation, the axial velocity at the free end of the ceramic rod was recorded for comparison with the experimental results of Wise and Grady (1994). In the unconfined ceramic rod experimental records, shown in Fig. 10, the velocity curve is shaped by the arrival of an initial compression, followed by a second compression wave that brought the surface velocity to its highest value on the order of 0.19 mm/μs, according to Wise and Grady (1994). The first wave travels at the ultrasonic longitudinal wave speed $C_L = 10.6$ mm/μs, while the second wave propagated at the calculated bar wave speed $C_B = 9.81$ mm/μs. After the velocity peaked, it decayed by about 20% to a relatively constant velocity. A similar velocity profile is observed in the case of the confined ceramic rod, only that this time the peak velocity is about 0.32 mm/μs. Two numerical simulations, unconfined and confined ceramic, are plotted in Fig. 10. The

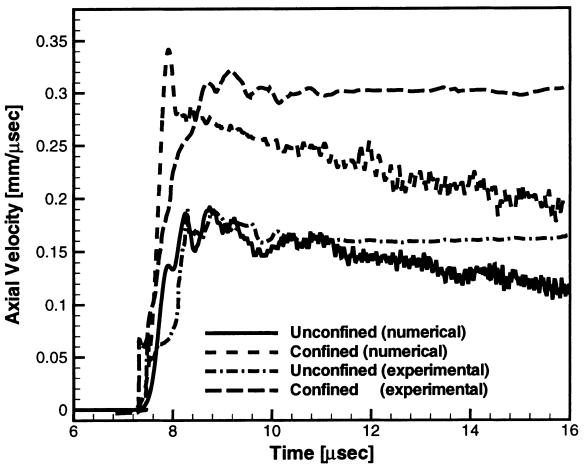

Fig. 10. Axial velocity on alumina bar free surface for both confined and unconfined ceramic bars.

calculated free surface velocity, in both numerical simulation, rises quickly to a peak on the order of 0.19 mm/μs and 0.34 mm/μs, respectively. In the numerical simulations, the wave arrival shows some retardation. This retarded arrival is likely due to the dispersion caused by the spatial discretization currently modeling the ceramic. In the case of unconfined ceramic, the first compressive pulse appears in the velocity trace, although its magnitude is about twice the magnitude of the experimentally recorded first compressive pulse. After the peak, the numerically computed velocities decay *progressively* to a mean value that is about 75% of the peak value. The continuous decay in axial free surface velocity is in contrast to the experimental records which show almost a constant axial velocity after the initial transient. The discrepancy is even more evident in the case of confined alumina. Espinosa and Brar (1995) showed that the almost constant axial velocity, at the ceramic bar end, is the result of ceramic spallation upon wave reflection at the ceramic rod free surface. This is also the case in the present simulations though the velocity never becomes constant.

The lack of a well defined elastic precursor in the numerically obtained axial velocity history, needs further investigation. It may be due, at least in part, to insufficient inelasticity in the ceramic model. In the present model, only microcracking is considered. It was shown by Espinosa et al. (1992), that the glassy phase present in the ceramic microstructure, can lead to a viscoplastic like behavior that can result in further wave front attenuation (precursor decay).

In Fig. 11, the radial velocity in the case of confined alumina, at 30 mm from the impact surface is plotted. In this figure both the experimental record and the numerical trace are shown. Despite a small overshoot of the peak radial velocity, the numerical solution captures the main features observed in the experimental trace. This agreement further

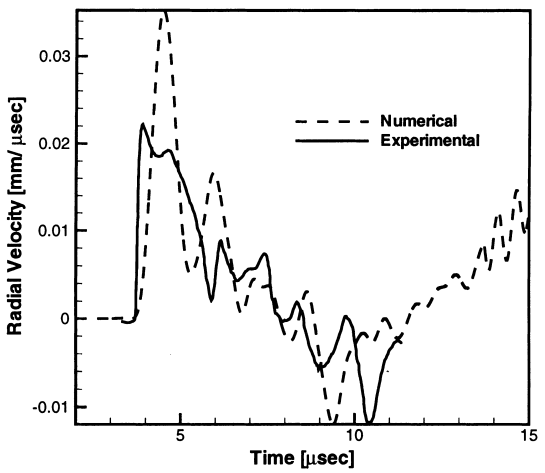

Fig. 11. Radial velocity of sleeve outer surface at 30 mm from the impact plane.

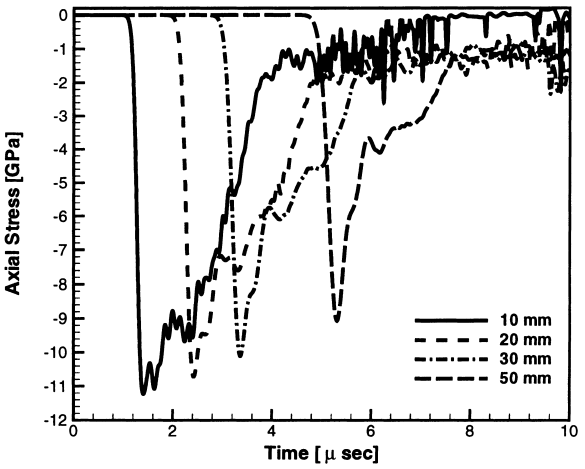

Fig. 12. Axial stress history in alumina bar for confined ceramic.

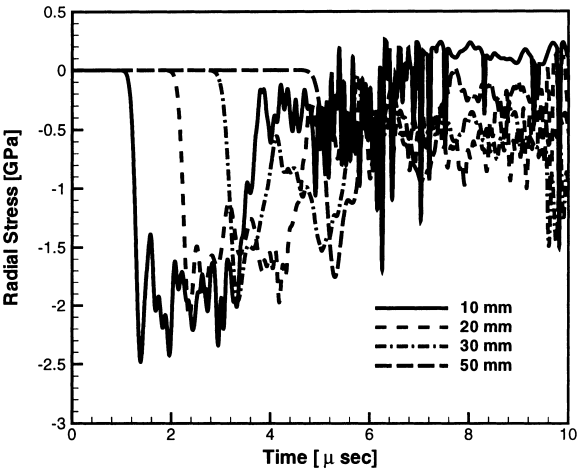

Fig. 13. Radial stress history at ceramic/tantalum interface.

show that the physics of damage and inelasticity are captured by the proposed models.

Further insight into the damage process, within the alumina bar, can be obtained from a plot of axial stress histories at various depths from the impact surface. In Fig. 12, these stress histories are plotted at a quadrature point located near the ceramic/tantalum interface. Several features can be observed. At 10 mm from the impact surface, the axial stress rapidly increases to a peak compressive stress of about 11 GPa. A progressive pulse decay follows with a total pulse duration of approximately 6 μs. Similar profiles are observed at stations farther away from the impact surface; although, the peak stress decays to a value of about 9 GPa at 50 mm. The decay and pulse shape are the result of damage and geometric effects (Espinosa and Brar, 1995). It should be noted, that the pulse shape plays an important role in the ceramic free end axial velocity, see Fig. 10. In fact, when a pulse with the shape shown in Fig. 12 reaches the bar free end, material spallation is expected to occur upon wave reflection.

The effectiveness of the tantalum sleeve, ceramic confinement, can be inferred from radial stress histories, see Fig. 13. In this figure, confinement stresses at the same quadrature points and depths from the impact surface are plotted. The traces reveal that at 10 mm from the impact surface, an average confinement of approximately 2 GPa is achieved for about 2.5 μs. After that, the stress decays significantly resulting in lost of confinement, ceramic–tantalum interface separation, at about 7 μs after impact. Similar features are observed at stations farther away from the impact surface. However, in contrast to the station at 10 mm, contact between the ceramic bar and tantalum sleeve is preserved in the first 10 μs. Since in the present configuration the confinement stress is mainly the result of Poisson's effect, a correlation between the axial stress histories and the confinement stress histories is observed.

6.3. Contours and mesh evolution

To illustrate the features included in the computational algorithm, mesh refinement and optimization, mechanical contact, and material inelasticity, a series of contour/mesh plots showing the state of the finite element calculation every 2 μs is presented. Figs. 14–17 are a series of contour plots showing the axial velocities throughout the rods, every 2 μs, for both confined and unconfined ceramic rods. As time progresses, we can see the stress wave move up the alumina rod (the upper rod) at a velocity of about 10,000 m/s. Notice that the alumina rod behaves in a more stiff manner than the plastically-deforming aluminum and tantalum rods, up until around 10 μs after impact. Then the elements

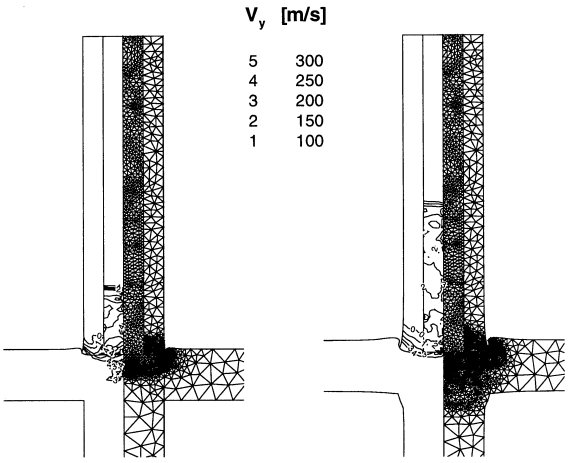

Fig. 14. Axial velocity contours at $t = 2$ and 4 μs.

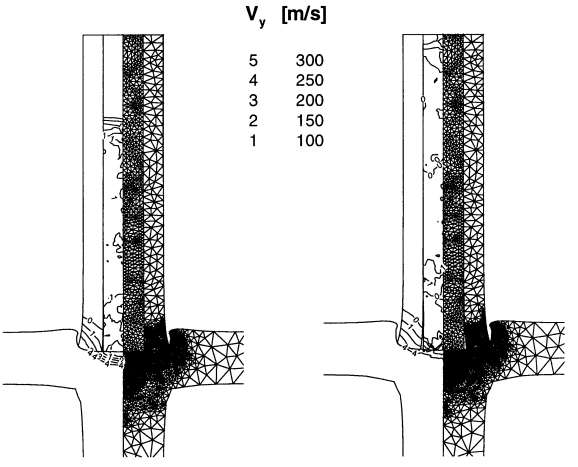

Fig. 15. Axial velocity contours at $t = 6$ and 8 μs.

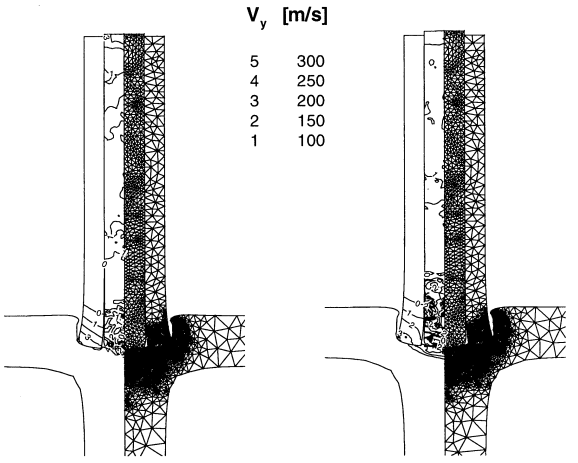

Fig. 16. Axial velocity contours at $t = 10$ and 12 μs.

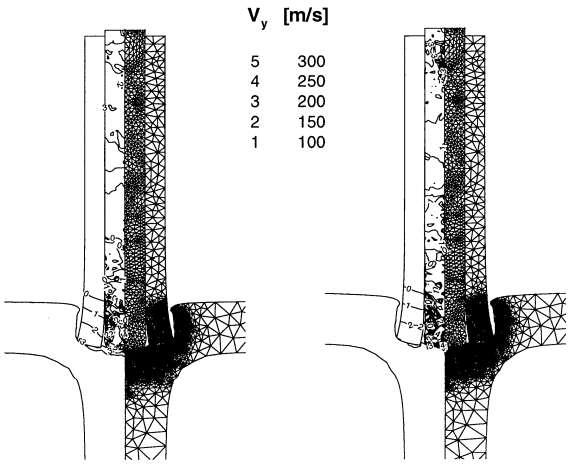

Fig. 17. Axial velocity contours at $t = 14$ and 16 μs.

at the end of the alumina rod reach a point in their state of cracking where they are essentially pulverized, and lose most of their stiffness. A wavy shape on the surface of the alumina rod is an indication of the degree of damage. Note that most of the inelastic deformation is concentrated in the elements on the very end of the rod and in a spall region near the upper end which trapped the rebounding tensile wave.

It is important to note that the severe damage accumulated in the alumina rod, in the proximity of the impact surface, becomes possible either by the absence of confinement or by the separation of the tantalum sleeve at about 7 μs, see Fig. 15. In the case of confined ceramic, the observed gap at the alumina–tantalum interface propagates away from the impact surface as seen in the sequence of mesh plots. This feature has a very important implication in the identification of damage and fragmentation. It shows that the metal sleeve can provide only partial confinement during the first 5–6 μs.

As expected, the aluminum anvil is cratered by the impact with the ceramic specimen, and provides a good test for the contact and remeshing capabilities of the algorithms presented in this paper.

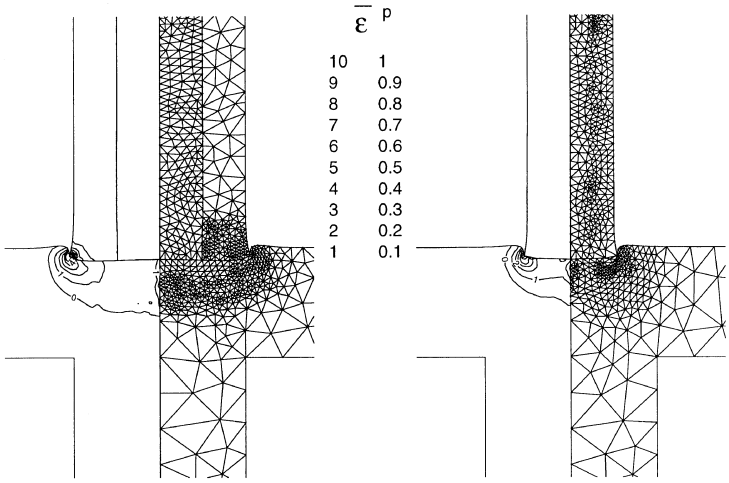

Fig. 18. Effective plastic strain contours at $t = 2$ μs.

The contact algorithm implemented in this calculation allows the aluminum to flow around the penetrating ceramic rod, gradually tracking the surfaces and redefining closest master nodes to reflect the physical problem. As deformation increases, the mesh refines itself several times automatically, using the rate of plastic work condition mentioned previously. Each time, all the elements with a work rate ratio of $\beta_{\max} > 1.1$ were refined. Note that elements that were smaller than $h_{\min} = 0.5$ mm across were not refined. One test of the interpolation and recomputation of the state variables due to a mesh rezoning is whether the mesh continues on after the rezoning without any sudden changes in the field variables. Upon examination of the velocity history in Fig. 10, it can be seen that no discontinuities in velocity or acceleration are introduced by mesh refinement. One interesting aspect of this problem is that the most rapid plastic deformation in the aluminum, as highlighted by the mesh refinement, is confined to a band of roughly constant width, instead of producing a smooth gradient over a larger area.

Also displayed, in Figs. 18–21, are contours of the effective plastic strain in the aluminum and tantalum rods at 2, 4, 6, and 8 μs into the calculation. The evolution of the mesh with automatic refinement and optimization, for both confined and unconfined ceramic, can be observed. Note that at 4 μs after collision, although the plastic strain is severe right near the surface, it possesses a fairly smooth gradient down to the low-strain regions. At 8 μs, however, the edge of the zone of large-scale plastic deformation has become well defined, where the effective plastic strain leaps from around 0.1 to greater than 1.0 in a very steep gradient. What is interesting is that the contours for the low strain (< 0.4) do not change very much between 6 and 8 μs. Most of the strain localizes in a band near the surface. Consistent with the formation of this band is the accumulation of small elements resulting from the mesh refinement algorithm previously discussed.

7. Concluding remarks

An adaptive finite element computation of geometric and material nonlinearities was presented within a unified framework. A total Lagrangian formulation was used to describe the field equations. Since Lagrangian approaches lead to excessive mesh distortions in finite deformation computations, algorithms for mesh rezoning, optimization, and refinement were implemented to efficiently advance the calculations in time. Contact between multiple-bodies was handled with an explicit contact scheme introduced by Taylor and

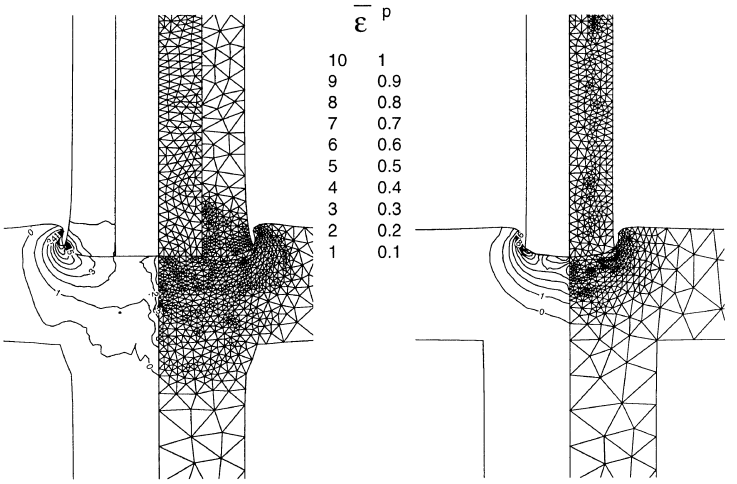

Fig. 19. Effective plastic strain contours at $t = 4$ μs.

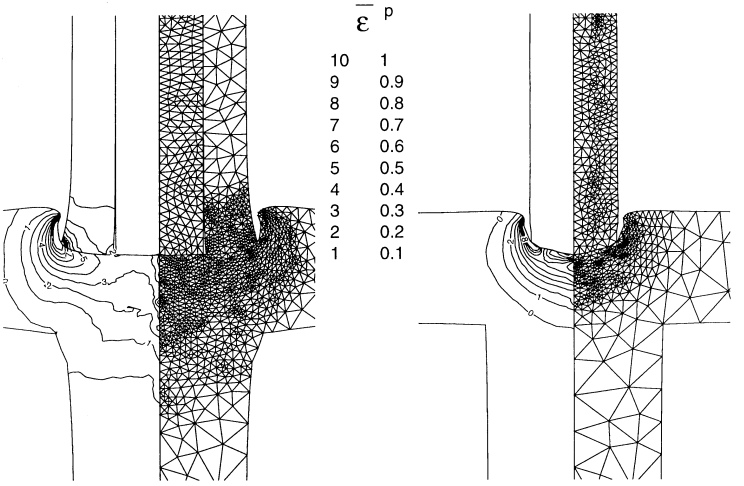

Fig. 20. Effective plastic strain contours at $t = 6$ μs.

Flanagan (1987). Extensions for the tratement of cohesive interfaces and heat fluxes between sliding bodies were also presented.

The various algorithms were implemented and tested in the analysis of brittle failure of ceramic rods, with and without confinement. Experiments reported by Wise and Grady (1994), were simulated through axisymmetric calculations. Damage in the ceramic was modeled by means of a multiple-plane microcracking model, while the plastic deformation of the aluminum impactor was modeled with a viscoplastic finite deformation model. Our simulations captured the physics of the problem and illustrated the effect of confinement in the failure of ceramics. Insight into the failure process was obtained through analysis of axial and radial velocity histories. Moreover, computed in-material stress histories improved our understanding of the effect of damage rate, and pulse shape and duration in the measured axial velocities. Difficulties in preserving the confinement, at late times, in a region close to the impact surface were also revealed

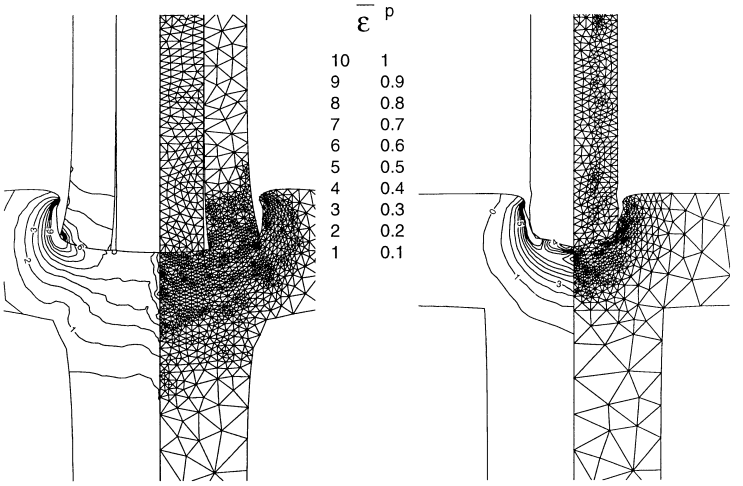

Fig. 21. Effective plastic strain contours at $t = 8$ μs.

by the calculations. As a result, fragmentation of the ceramic rod, in a fashion similar to the fragmentation observed in high speed photography of unconfined ceramic rods (Espinosa and Brar, 1995) could be expected.

It should be noted that, due to tilt, the rod on rod impact experiment is a 3-D problem. Since fragmentation of brittle materials may be strongly sensitive to tilt, our axisymmetric approximation may not have captured all the features present in the experimental records reported by Wise and Grady (1994). This and other challenges in the modeling of brittle materials still remain. A model coupling plasticity and microcracking seems to be needed for a proper description of the early stages of inelasticty including the determination of crack densities. Early inelasticity is believed to be responsible for the masured elastic precursors. Although we have shown that a continuum damage model can capture ceramic inelasticity quite well, and that measured velocity profiles can be reproduced with a multiple-plane microcracking model, real applications may require analysis of the transition from a continuum to multi bodies as a result of material fragmentation. In principle, the contact/cohesive interface model proposed in this paper could be used for such analyses. However, a well thought out scheme for the transition is required to properly represent the physics of fragmentation without a priori assumptions on fragment sizes which may lead to mesh dependent results.

Acknowledgements

This research was supported by the National Science Foundation through Grants Nos. MSS-9309006, MSS 9311289, CMS-9523113, and by the Army Office of Scientific Research through Grant No. DAAH04-96-1-0142. The first author wishes to thank M. Ortiz and A. Cuitiño for providing valuable insight into the implementation of the large deformation plasticity algorithm.

References

Asaro, R.J., Rice, J.R., 1977. Strain localization in ductile single crystals. J. Mech. Phys. Solids 25, 309.

Atluri, S.N., 1984. Alternate stress and conjugate stress measures, and mixed variational formulations involving rigid rotations, for computational analysis of finitely deformed solids, with application to plates and shells: I. Theory. Computers Struct. 18, 93–116.

Bathe, K.-J., 1996. Finite Element Procedures. Prentice-Hall, Englewood Cliffs, NJ.

Batra, R.C., Hwang, J., 1993. An adaptive mesh refinement technique for two-dimensional shear band problems. Comp. Mech. 12, 255.

Batra, R.C., Kuo, K.I., 1992. An adaptive mesh refinement technique for the analysis of shear bands in plane strain compression of a thermoviscoplastic solid. Comp. Mech. 10, 369.

Bazant, Z.P., Gambarova, P.G., 1984. Crack shear in concrete: crack band microplane model. J. Struct. Eng. ASCE 110 (9), 2015.

Belytschko, T., 1983. An overview of semidiscretization and time integration procedures. In: Belytschko, T., Hughes, T. (Eds.), Computational Methods for Transient Analysis, p. 301.

Benson, D.J., 1992. Computational methods in Lagrangian and Eulerian hydrocodes. Comput. Methods Appl. Mech. Eng. 99, 235.

Clifton, R.J., Klopp, R.W., 1985. Pressure-shear plate impact testing. In: Metals Handbook: Mechanical Testing 8, 9th edition. American metal society, p. 230.

Donea, J., 1983. Arbitrary Lagrangian–Eulerian finite element methods. In: Belytschko, T., Hughes, T. (Eds.), Computational Methods for Transient Analysis, p. 473.

Duffy, J., 1979. The dynamic plastic behavior of structural materials: A review. Prepared for the Engineering Foundation.

Dvorkin, E.N., Petocz, E.G., 1992. On the modelling of 2D metal forming processes using flow formulation and the pseudo-concentration technique. In: Owen, D.R.J., Oñate, E., Hinton, E. (Eds.), Proceedings of Third International Conference on Comput. Plasticity, p. 1037.

EPIC, 1996. User Instructions for the Final Version of the EPIC Research Code. by Johnson, G.R., Stryk, R.A., Petersen, E.H., Holmquist, T.J., Schonhardt, J.A., Burns, C.R. Alliant Techsystems Inc., 600 Second St. N.E., Hopkins, MN 55343.

Espinosa, H.D., 1989. Finite element analysis of stress induced damage in ceramics. M.Sc. Thesis, Brown University, Providence, RI.

Espinosa, H.D., 1995. On the dynamic shear resistance of ceramic composites and its dependence on applied multiaxial deformation. Int. J. Solids Structures 32 (21), 3105–3128.

Espinosa, H.D., Brar, N.S., 1995. Dynamic failure mechanisms of ceramic bars: Experiments and numerical simulations. J. Mech. Phys. Solids 43 (10), 1615.

Espinosa, H.D., Clifton, R.J., 1991. An experimental investigation of inelasticity in shock loaded AlN/Al composites. In: Kim, K.S. (Ed.), Experiments in Micromechanics of Failure-Resistant Materials, ASME Special Technical Publication AMD-130, Atlanta, Georgia, pp. 37–56.

Espinosa, H.D., Raiser, G., Clifton, R.J., Ortiz, M., 1992. Experimental observations and numerical modeling of inelasticity in dynamically loaded ceramics. J. Hard Mater. 3 (3/4), 285–313.

Espinosa, H.D., Emore, G., Xu, Y., 1995. High strain rate behavior of composites with continuous fibers. In: Rajapakse, Y.D.S., Vinson, J.R. (Eds.), High Strain Rate Effects on Polymer, Metal and Ceramic Matrix Composites and Other Advanced Materials, ASME Special Technical Publication, San Francisco, California, p. 6.

Espinosa, H.D., Lu, H.C., 1995. Unpublished research.

Flanagan, D.P., Belytschko, T., 1984. Eigenvalues and stable time steps for the uniform strain hexahedron and quadrilateral. J. Appl. Mech. 51, 35.

Freund, L.B., 1990. Dynamic Fracture Mechanics. Cambridge University Press, Cambridge.

Grady, D., 1995. Dynamic properties of ceramic materials. Sandia Report, SAND94-3266.

Havner, K.S., 1973. On the mechanics of crystalline solids. J. Mech. Phys. Solids 38, 87.

Hauver, G.E., Netherwood, P.H., Benck, R.F., Kecskes, L.J., 1994. Enhanced ballistic performance of ceramics. In: Nineteenth Army Science Conference, Orlando, Florida, 20–24 June.

Hill, R., Rice, J.R., 1972. Constitutive analysis of elastic-plastic crystals at arbitrary strain. J. Mech. Phys. Solids 20, 401.

Hughes, T.J.R., 1987. The Finite Element Method. Prentice-Hall, Englewood Cliffs, NJ.

Ju, J.W., Lee, X., 1991. Micromechanical damage models for brittle solids. I.J. Eng. Mech. ASCE 117 (7), 1995.

Komanduri, R., 1993. Machining and grinding: A historical review of the classical papers. Appl. Mech. Rev. 46 (3), 80.

Lee, E.H., 1969. Elastic plastic deformations at finite strains. ASME J. Appl. Mech. 36, 1–6.

Liu, W.K., Chang, H., Chen, J.S., Belytschko, T., 1988. Arbitrary Lagrangian–Eulerian Petrov–Galerkin finite elements for nonlinear continua. Comput. Methods Appl. Mech. Eng. 68, 259.

Longy, F., Cagnoux, J., 1989. Plasticity and microcracking in shock-loaded alumina. J. Am. Ceram. Soc. 72 (6), 971.

Lubliner, J., 1990. Plasticity Theory. Macmillan, New York.

Mandel, J., 1972. Plasticité classique et viscoplasticité. Course given at Int. Center for Mech. Sci., Udine, Springer, Berlin.

Marusich, T.D., Ortiz, M., 1995. Modelling and simulation of high-speed machining. Int J. Numer. Methods Eng. 38, 3675.

Nagtegaal, J.C., Parks, D.M., Rice, J.R., 1974. On numerically accurate finite element solutions in fully plastic range. Comput. Methods Appl. Mech. Eng. 4, 469–484.

Needleman, A., 1988. Material rate dependence and mesh sensitivity in localization problems. Comput. Methods Eng. 67, 69.

Nicholas, T., Rajendran, A.M., 1990. Material characterization at high strain rates. In: Zukas, J.A. (Ed.), High Velocity Impact Dynamics. Wiley, New York.

Ortiz, M., Quigley, J.J., 1991. Adaptive mesh refinement in strain localization problems. Comp. Methods Appl. Mech. Eng. 90, 781.

Oxley, P.L.B., 1989. Mechanics of Machining. Ellis Horwood, Chichester.

Özisik, M.N., 1977. Basic Heat Transfer. McGraw-Hill, New York.

Rajendran, A.M., 1992. High strain rate behavior of metals, ceramics, and concrete. Air Force Report WL-TR-92-4006, Wright-Patterson Air Force Base, OH.

Rice, J.R., 1971. Inelastic constitutive relations for solids: An internal-variable theory and its application to metal plasticity. J. Mech. Phys. Solids 19, 433.

Rosenberg, Z., Yeshurun, Y. Brandon, D.G., 1985. Dynamic response and microstructure of commercial alumina. In: Proceedings of International Conference Mech. Phys. Behavior Mat. under Dynamic Loading; J. Phys. C5 (8), 331.

Sandler, I.S., Wright, J.P., 1984. Strain-softening. In: Nemat Nasser et al. (Eds.), Theoretical Foundations for Large Scale Computations of Nonlinear Materials Behavior, p. 285.

Seaman, L., Dein, J.L., 1983. Representing shear band damage at high strain rates. In: Proceedings of IUTAM Symposium on Nonlinear Deformation Waves, Tallin, Estonia. Springer, Berlin.

Shih, A.J., Yang, H.T., 1993. Experimental and finite element predictions of residual stresses due to orthogonal metal cutting. Int. J. Numer. Methods Eng. 36, 1487.

Simha, C.H.M., Bless, S.J., Brar, N.S., 1995. Dynamic failure of AD99.5 alumina. In: Murr, L.E., Staudhammer, K.P., Meyers, M.A. (Eds.), Metallurgical and materials applications of shock-wave and high-strain-rate phenomena. Elsevier, New York, pp. 195–202.

Stillman, D.W., Lum, L., Hallquist, J.O., Benson, D.J., 1993. An arbitrary Lagrangian–Eulerian capability for LS-DYNA3D. AMD 171, 67.

Sundaram, S., Clifton, R.J., 1996. Pressure-shear impact investigation of the dynamic response of ceramics. In: Clifton, R.J., Espinosa, H.D. (Eds.), Advances in Failure Mechanisms in Brittle Materials, Atlanta, Georgia. ASME Special Technical Publication MD-75/AMD-219, pp. 59–80.

Taylor, L.M., Flanagan, D.P., 1987. PRONTO 2D: A two-dimensional transient solid dynamics program. Sandia Report SAND86.

Teodosiu, C., 1970. A dynamic theory of dislocations and its applications to the theory of elastic-plastic continuum. Fundamental Aspects of Dislocation Theory, 2, National Bureau of Standards (US) Special Publication, p. 837.

Tvergaard, V., 1990. Effect of fibre debonding in a whisker-reinforced metal. Mater. Sci. Eng. A 125, 203.

Weber, G., Anand, L., 1990. Finite deformation constitutive equations and a time integration procedure for isotropic, hyperelastic-viscoplastic solids. Comp. Methods Appl. Mech. Eng. 79, 173.

Wise, J.L., Grady, J.R., 1994. Dynamic, multiaxial impact response of confined and unconfined ceramic rods. In: Schmidt, S.C., Shaner, J.W., Samara, G.A., Ross, M. (Eds.), Proceedings of High Pressure Science and Technology, APS Meeting, p. 777.

Yang, H.T., Heinstein, M., Shih, J.M., 1989. Adaptive 2D finite element simulation of metal forming processes. Int. J. Numer. Methods Eng. 28, 1409.

Zavattieri, P.D., Buscaglia, G.C., Dari, E.A. Finite element mesh optimization in three dimensions, submitted.

Zavattieri, P.D., Dari, E.A., Buscaglia, G.C., 1996. Optimization strategies in unstructured mesh generation. Int. J. Numer. Methods in Eng. 39, 2055–2071.

Zavattieri, P.D., 1995. Finite element mesh optimization in three dimensions. M.Sc. Thesis, Instituto Balseiro, Argentina.

Zhou, M., Ravichandran, G., Rosakis, A.J., 1996. Dynamically propagating shear bands in impact-loaded prenotched plates – II. Numerical simulations. J. Mech. Phys. Solids 44 (6), 1007.

Zhu, J.Z., Himton, E., Zienkiewicz, O.C., 1991. Adaptive finite element analysis with quadrilaterals. Comput. Struct. 40 (5), 1097.

Zienkiewicz, O.C., Taylor, R.L., 1991a. The Finite Element Method, vol. 1, 4th edition. McGraw-Hill, New York.

Zienkiewicz, O.C., Taylor, R.L., 1991b. The Finite Element Method, vol. 2, 4th edition. McGraw-Hill, New York.

Zukas, J.A., 1990. High Velocity Impact Dynamics. Wiley, New York.